Journal of Hydrology 626 (2023) 130316

Contents lists available at ScienceDirect

Journal of Hydrology

journal homepage: www.elsevier.com/locate/jhydrol

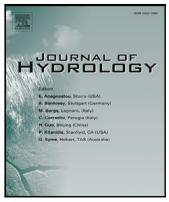

Research papers

Long-term hydrological behavior of an Alpine glacier

Maria Grazia Zanoni [a,b], Elisa Stella [c], Alberto Bellin [a,*]

[a] Department of Civil, Environmental and Mechanical Engineering, DICAM, University of Trento, Via Mesiano 77, I-38123 Trento, Italy
[b] Department of Environmental Systems Science, ETH Zürich, Universitätstrasse 16, 8092 Zürich, Switzerland
[c] Department of Environmental Sciences, Informatics and Statistics, Ca' Foscari University of Venice, Scientific Campus, Via Torino, 155, 30172, Mestre-Venice, Italy

ARTICLE INFO

This manuscript was handled by Marco Borga, Editor-in-Chief, with the assistance of Francesco Avanzi, Associate Editor.

Dataset link: https://data.mendeley.com/datasets/z4b439psmn/1

Keywords:
Glacial runoff
Hydrological alterations
Alpine glaciers
Deep Neural Network
Climate change

ABSTRACT

Alpine glaciers are shrinking at a relentless pace, as an effect of global warming. The impact of these changes in the European Alps is relevant, given the importance of this territory from both ecological and economic viewpoints. While the ubiquitous reduction of glaciers' mass through the Alps has been reported in several studies, its effect on streamflow is less studied. In the present work, we analyzed the long streamflow time series, available since 1976, of the Careser Stream, a headwater stream emerging from the Careser Glacier, in northeastern Italy. A large amount of missing data characterizes the streamflow time series, which we filled with a high level of confidence by using a Feed Forward Deep Neural Network algorithm. We explored the influence of climatic drivers on streamflow at monthly and annual time scales. Our analysis highlighted significant changes in the timing of streamflow due to the combined effect of early snow melting and a progressive reduction of the glacier's area. The hydrological regime changed significantly with glacier water contributing to streamflow proportionally less after a tipping point identified in 1996. Projections performed by using eight bias-corrected climate models of the EURO-CORDEX collections confirmed this tendency with the complete transition of the catchment from the glacial to the nival regime by 2045 at the latest. The Deep Neural Network algorithm was very effective in filling the missing streamflow data and this offers an encouraging premise for applications in other glaciers of the Alps suffering from the same transformation.

1. Introduction

The relevant role of climate change on hydrological alterations in snow- and glacial-dominated mountain catchments is widely recognized worldwide (see e.g., Baraer et al., 2012; Huss and Hock, 2018; Marzeion et al., 2020; Immerzeel et al., 2020; Hugonnet et al., 2021), and in the European Alps (Beniston, 2003; Barnett et al., 2005; Gobiet et al., 2014; Majone et al., 2016; Zekollari et al., 2019) in particular, where summer meltwater from glaciers contributes significantly to the downstream river flows (Kuhn and Batlogg, 1998; Jansson et al., 2003; Huss, 2011; Carturan et al., 2019; Mallucci et al., 2019; Bolibar et al., 2022).

Recent analyses showed that changes in the precipitation pattern and the contemporaneous rise of air temperature have led to a rapid melting of glaciers, which is considered a major cause of alteration of the typical nivo-glacial regime of the Alpine headwaters (Birsan et al., 2005; Kormann et al., 2015; Hugonnet et al., 2021; Laurent et al., 2020; Galos et al., 2015; Michel et al., 2020). Alpine glaciers, with observations dating back to 1850 (Paul et al., 2004), are among those showing the most negative mass balances of the entire globe (Bliss et al., 2014). According to recent estimates (Paul et al., 2011), glaciers and ice patches of the European Alps shrunk to 1/3 of the surface they occupied in the 1970s, resulting in an average area loss rate of about 2% per year. Other studies (Haeberli et al., 2007; Huss, 2012; Carturan et al., 2016) claimed that current rates of glaciers retreat are of the order of 1 m of water equivalent per year, well above the long-term average, thereby indicating that the melting rate is accelerating.

Despite these evidences, catchment scale hydrological alterations due to changes in glacier mass balance received less attention than glacier mass loss or global effects due to the melting of large glacierized areas (Milner et al., 2017; Huss and Hock, 2018; Marzeion et al., 2020; Immerzeel et al., 2020; Hugonnet et al., 2021). Available studies on hydrological alterations address specific glacier systems (Jost et al., 2012; James D. Miller, 2012; Kure et al., 2013; O'Neel et al., 2014; Nepal, 2016) with an emphasis on assessing future scenarios (see e.g., Huss et al., 2008; Koboltschnig et al., 2008; Weber et al., 2010; Farinotti et al., 2012; Bavay et al., 2013). Among these contributions, those analyzing observational data (Gurnell et al., 1992; Collins, 2006, 2008; Schädler and Weingartner, 2010; Grossi et al., 2013) are less in

* Corresponding author.
E-mail address: alberto.bellin@unitn.it (A. Bellin).

https://doi.org/10.1016/j.jhydrol.2023.130316
Received 14 September 2022; Received in revised form 9 September 2023; Accepted 27 September 2023
Available online 14 October 2023

number and often based on relatively short time series. Long-term time series facilitate the assessment of hydrological alterations, particularly those caused by climate change, which are difficult to disentangle from other effects when only short-term time series are available (Bunn and Arthington, 2002; Poff and Zimmerman, 2010; Jacobsen et al., 2012; Brown et al., 2015; Milner et al., 2017; Brown et al., 2007). Unfortunately, long-term streamflow time series are rare, because of the difficulties in maintaining streamflow gauges at high elevations.

To explore the hydrological changes occurring in a representative glacier of the Southern Alps, we analyzed the long-term streamflow time series of the stream emerging from the Careser Glacier and bearing the same name. With monitoring activities documented since the end of the 19th century, this glacier is one of the most extensively monitored in the southern Alps (Zanon, 1992; Carturan and Seppi, 2007; Carturan et al., 2013a,b, 2016; RGI Consortium, 2017), and therefore it represents an important source of information to study the effects of climate change in Alpine glaciers. Mass balance has been performed annually since 1967 and for this reason, the Careser has been classified as one of the reference glaciers by the World Glacier Monitoring Service (Zemp et al., 2015).

We investigated the ongoing changes in the glacier hydrological regime by performing a comprehensive analysis of multiscale variations of precipitation, temperature, flow rate, and glacier mass. In the analysis, we complemented available meteorological data with spatial geostatistical models of air temperature and precipitation, with the parameters inferred by minimizing the model's error at a meteorological station close to, but at a lower elevation than the glacier. In addition, we reliably reconstructed the discontinuous streamflow measurements with a Deep Dense feed-forward Neural Network (DNN) model trained on the available data. This model was also effective in evaluating the near future evolution of the glacier by using the simulations of eight Climate change models as input. We showed that these approaches are valuable tools for the hydrological modeling of mountain glaciers, where data are often scarce and discontinuous.

2. Study area

The Careser Glacier (Fig. 1) is located on the south-eastern reach of the Ortles-Cevedale group, in the upper Pejo valley (Val di Pejo), northwest of the city of Trento, Italy. In 2015, the glacier was occupying a portion (1.39 km^2) of a large, south-facing, circle between 2910 and 3275 m a.s.l. and it was composed of a main ice body and five smaller patches of varying extensions (see Fig. 1) (Carturan et al., 2013a,b; WGMS, 2017).

The current aspect of the glacier is the result of dramatic changes that occurred chiefly in the last three decades. At the beginning of the 20th century, the glacier covered an area of about 5.4 km^2 with its tongue reaching the Careser reservoir, which has been in operation since 1934, more than 2 km downstream of the actual position (Carturan et al., 2013a). By 1958, the glacier lost its southern offshoot, and in 1959 its area diminished to 4.74 km^2 (see Figure 6 and Table 2 in Carturan et al. (2013a) and Fig. 1). In the following three decades the glacier was relatively stable and reached an extension of 4.57 km^2 in 1987 (Carturan et al., 2013a) before experiencing a dramatic decline of its surface to 1.39 km^2 in 2015, with a loss of 70% of its 1987 extension (Fig. 1).

Snow accumulates on the glacier chiefly in winter by direct precipitation and wind-drifted snow. In the late spring and summer seasons, meltwater feeds the Careser Stream, which after about 2 km enters the Careser reservoir with a drainage area of 8.5 km^2. Consequently, the glacier occupied 57% of the catchment in 1958 and only 16% in 2015.

3. Data

3.1. Meteorological and hydrological data

The Careser Stream was monitored since 1920, to obtain the data needed, initially for the design of the Malga Mare hydropower system, and later for supporting the production strategies of the company. The Malga Mare hydropower system is fed by the Careser reservoir located about 2 km downstream of the actual glacier snout. During the construction of the hydropower system, completed in 1934, a meteorological station was installed near the dam at the elevation of 2600 m a.s.l. (T0065, 46° 25′ 30.4ε N, 10° 41′ 57.5ε E in WGS 84, hereafter indicated with the commonly used local name of Careser Diga). Regular measurements of daily maximum (T_{max}) and minimum (T_{min}) air temperatures are available at the Careser Diga station since 1939 and from 1990 air temperature was measured at 15-minute time steps. On September 2, 2011, MeteoTrentino installed a new meteorological station in the area occupied by the glacier (T0437, 46°27′ 04.4ε N, 10°43′05.5ε E in WGS 84, 3093 m a.s.l., Fig. 1). This station recorded air temperature at a 15-minute time step, as the Careser Diga station. Daily precipitation measurements started in 1929 at the Careser Diga and since 1990 they have been recorded at a 15-minute time step.

A stream gauge was installed at the location called Careser Baia, just upstream of the reservoir at the elevation of 2642 m a.s.l. and later equipped with an automatic water stage sensor (T0308, 46° 25′ 44.4ε N, 10°42′ 19.2ε E in WGS 84). Because of the prevailing freezing conditions, this gauging station operates only from May to October, with starting and ending dates changing due to interannual climate variability. From 1976 to 2002 water stage was recorded every 15 min and successively every 5 min.

The time series of the gauging station T0308 was obtained from MeteoTrentino (2023). In addition, air temperature and precipitation at station T0065 and 32 neighborhood stations were obtained from MeteoTrentino (2023, In: "Dati e Osservazioni → DATI STORICI → Elenco Stazioni") and Weather South Tyrol (2023). These meteorological stations were selected as described in Appendix A and were used for gap filling of the Careser Diga station (T0065) time series and modeling the daily temperatures at the glacier.

Future projections were obtained as described in Section 4.2 by using precipitation and temperatures extracted from eight climate models of the EURO-CORDEX ensemble. The projections were performed under the scenarios RCP 4.5 and RCP 8.5 adopted by the Intergovernmental Panel on Climate Change (IPCC) and corresponding to the intermediate and pessimistic scenarios, respectively. The four General Climate Models employed are the following, with the respective combined four Regional Climate Models indicated within brackets: CNRM-CM5 (CCLM4-8-17), EC-EARTH (CCLM4-8-17, HIRHAM5, RACMO22E), HadGEM2-ES (CCLM4-8-17, RACMO22E), MPI-ESM-LR (CCLM4-8-17, REMO2009).

3.2. Glaciological and topography data

Long-term (1967–2020) observations of winter accumulation (C_w, [mm w.e.]), summer ablation (A_s, [mm w.e.]) and net mass balance (B_n, [mm w.e.]) together with the Equilibrium Line Altitude (ELA) of the Careser Glacier, were provided by MeteoTrentino (2023, In: "Neve e ghiacci → DATI GLACIOLOGICI (Bilanci di Massa)"). These data stem from analyses of measurements at ranging rods, placed between 2900 *m a.s.l.* and 3200 *m a.s.l.*, performed by the University of Padova, for the period 1967–2001 (Zanon, 1992), and by the University of Padova in collaboration with MeteoTrentino for the following years (see e.g. Carturan and Seppi, 2007, for a description of the activities performed and the data collected).

Digital Terrain Models (DTMs), of the years 1994, 2003, and 2007, orthophotos of the years 1980, 1987, 1990, 2000, 2003, 2006, and 2015, and georadar measurements performed in 2007 and 2008 were used to determine the evolution of the glacier extension (see Section 6 and Appendix C). DTMs and orthophotos were provided by MeteoTrentino (2023) and georadar measurements were presented in previous works (see Martinelli et al., 2010; Carturan et al., 2013b).

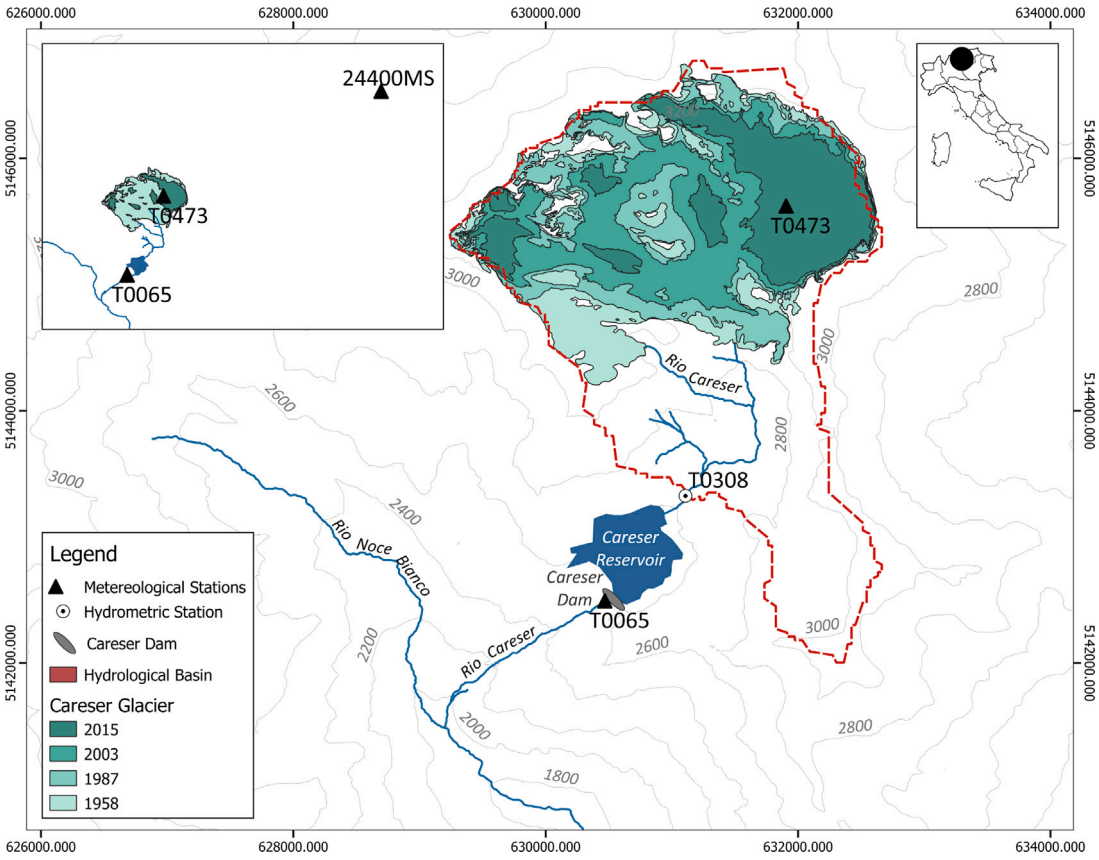

Fig. 1. Time evolution of the Careser Glacier. Coordinates are in the system UTM-WGS 84 (zone 32N) and surface topography is indicated with contour lines with elevations expressed in m a.s.l.. The positions of the Careser Diga (T0065) and glacier (T0473) meteorological stations as well as the Careser Baia stream gauge station (T0308) and the reservoir are also indicated.

4. Methods

4.1. Reconstruction and modeling of missing data

Meteorological and streamflow time series, collected as described in Section 3, were incomplete with gaps of varying extension due to temporary malfunctioning of the sensors and inactivity of the stream gauging station in the winter season from about the middle of October to May–June. In addition, very few measurements are available at the glacier. The percentage of available daily values of the time series between 1976 and 2020 are shown in Fig. 2. At station T0065, temperatures show relatively few gaps at the daily scale (between 7% and 8%) and similarly the daily precipitations (7.83%). The situation is more problematic for the streamflow at station T0308 with 58% of daily flow rates that are missing in the summer period from May to October. Therefore, before performing any analysis of the available data the time series were gap-filled as specified below. In addition, the temperatures at the glacier were modeled by using the geostatistical model described in Section 4.1.1.

4.1.1. Kriging with external drift

The Kriging with External drift (KED) model was employed for gap-filling the daily air temperatures (T_{max}, T_{min} and T_{mean}) and the monthly precipitation (P) at the Careser Diga (T0065) and also for modeling the spatial mean of the daily temperatures at the glacier. These time series were successively used for the reconstruction of the daily flow rates at the gauging station T0308 performed by the DNN algorithm as detailed in Section 4.1.2

Modeling with KED was performed separately for P, T_{max}, T_{min} and $T_{mean} = (T_{max} + T_{min})/2$ by using the elevation as secondary exhaustive information (Goovaerts et al., 1997). KED is described in Appendix A,

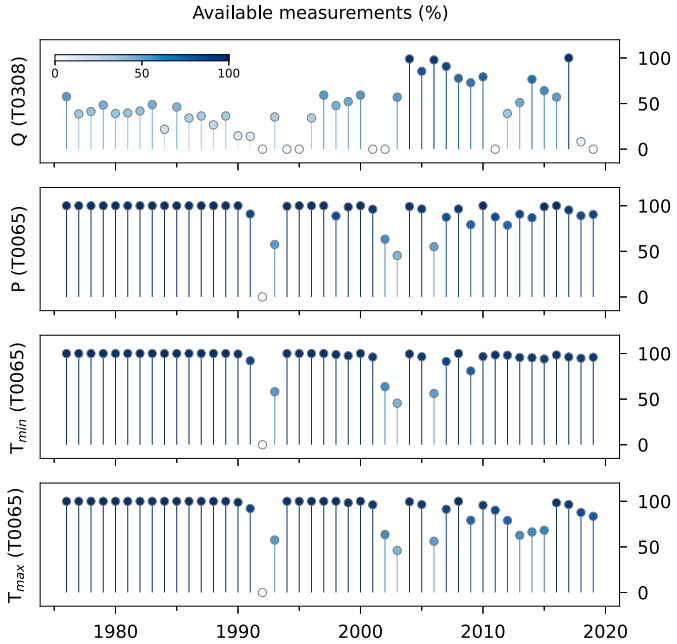

Fig. 2. Percentage of available daily temperatures, precipitation, and flow rate. For the flow rate (Q), only the summer days (from May 1 to October 31) were considered.

together with the methodology employed for the optimal inference of the model's parameters and hyper-parameters obtained by assuming the station T0065 as reference. Notice that the hyper-parameters were set

the same for all the modeled variables, while the covariance parameters were specific for each variable. The resulting KED models were then used for gap-filling the time series at the Careser Diga (T0065) and modeling the spatial mean of the daily temperatures at the glacier. The latter was obtained by averaging the modeled temperatures at the center of the squared cells, with a size of 150 m, of the grid delimited by the glacier contour in the year 1987. The same model applied to the smaller domain of the glacier in 2015 led to negligible differences in the daily temperatures, thereby the former was used for the successive analysis and the reconstruction of the flow rate at the Careser Baia station.

4.1.2. Streamflow reconstruction and modeling

Streamflow was available at the Careser Baia gauging station (T0308, Fig. 1), which includes runoff from both the glacier and the intermediate non-glacial catchment. At this station the flow rate was obtained from water stage measurements employing the following rating curve: $Q = a\,h^b$, where h is the measured water stage and the coefficients $a = 10.7473$ and $b = 1.15787$ were computed as described in Appendix D. A significant amount of gaps were observed in the active periods from May to October as reported in Fig. 2 and they were filled as described below. The water stage had been recorded since 1976 at a time step of 15′ with a sensor that was active between May and October when environmental conditions were favorable.

Before gap filling, the flow rate was aggregated at the hourly scale, discarding the intervals with less than 75% sub-hourly measurements, and successively at the daily scale, with the same criteria, i.e. discarding intervals with less than 19 hourly values. The resulting gaps in the daily streamflow time series were filled by using the DNN algorithm. The reconstruction was extended to the winter period (from November to April) for the purpose of wavelets analysis, but only the data from May to October were used in the other analyses. A detailed description of the DNN algorithm, including the procedure adopted for splitting the database into training and test sets, as well as the cross-validation procedure used to obtain the optimal values of the hyper-parameters (the number of layers and the number of neurons), is provided in the Appendix B.

The DNN was applied with the following input variables: (i) solid and liquid daily precipitations at the Careser Diga (T0065), considering as threshold for separating them a daily mean air temperature of 0 °C; (ii) spatial mean of daily minimum and maximum air temperatures at the glacier computed as described above and in the Appendix A; (iii) the Julian day and finally (iv) the daily ablation volume estimated as $v_A = V_A/184$, where $V_A = A_s\,A_g$ is the volume of summer ablation given by the product of the summer ablation $A_s\,[L]$ and the glacier surface, $A_g\,[L^2]$. v_A was assumed the same for all the days of the summer period (1 May–31 October), and it was considered equal to zero in the winter period. The same DNN model fed with the meteorological variables obtained from the climate models was used in Section 4.2 to obtain future streamflow scenarios in the ablation period.

4.2. Future projections

The projected future evolution of the Careser Glacier and the associated streamflow were investigated by using the EURO-CORDEX ensemble climate models with the future scenarios RCP 4.5 and RCP 8.5. Temperature and precipitation projected by the climate models for the period 2020–2070 were bias corrected by the Quantile Mapping method by using the Python library *biascorrection* (Kumar, 2020). This method is widely applied in the correction of the biases models (see e.g. Dobler and Ahrens, 2008; Jakob Themeßl et al., 2011; Piani et al., 2010). The projected precipitations were considered solid when the mean daily temperature was ≤ 0 °C and liquid otherwise.

The projections were employed to obtain the future evolution of the glacier area and the streamflow during the ablation season, as follows. First, the model of summer ablation was obtained by linear regression of the measured ablation A_s^* in the period 1976–2020 with the mean summer temperature ($\overline{T}_{sum}$): $A_s^* = 512.22 + 1007.7\,(\overline{T}_{sum})$ ($R^2 = 0.6214$, and $p = 0.0$ for both the regression coefficients). This model was used with the mean summer temperature of the climate models to project the future summer ablation, and the ablation volume as well, after multiplication by the glacier area. The latter was obtained from the area versus thickness graph of Fig. C.1 after updating the glacier thickness as follows: $h_{g,i} = h_{g,i-1} - (A_{s,i} - P_{w,i})$, where $A_{s,i}$ is the summer ablation (obtained from the temperature with the above regression curve), $P_{w,i}$ is the cumulative winter solid precipitation, and i indicates the time step. The resulting evolution in time of the glacier area and the flow rate are shown in Fig. 14a and 14b, respectively, for the following three cases: the ablation A_s^* predicted by the regression curve (scenario A1 in Fig. 14) and two additional values $A_s^* + \sigma$ and $A_s^* - \sigma$ (scenarios A2 and A3, respectively), with $\sigma = \sqrt{\frac{\sum_1^{N_a}(A_{s,i} - A_{s,i}^*)^2}{N_a}}$, where N_a is the number of measurements used in the regression.

4.3. Quality of the models

The accuracy of the KED and DNN models, respectively at Careser Diga (T0065) and at the Careser Baia (T0308), was assessed by the Nash Sutcliffe coefficient:

$$NS = 1 - \frac{\sum_{i=1}^{n}\left[z_i^* - z_i\right]^2}{\sum_{i=1}^{n}\left[z_i - \overline{z}\right]^2} \tag{1}$$

where z_i indicates the observed value at the $i-$th time step of the reference time series and z_i^* the corresponding modeled value. Furthermore, $\overline{z}$ is the mean of the n observed values. In doing this the reference station (T0065) was removed from the pool of neighborhood stations used in the KED.

4.4. Homogeneity test and trend analysis

Gap-filling at the Careser Diga station was performed by adding to the measured time series the values provided by the KED model at the time steps of the missing values. The NS values of the modeled P (at monthly scale), T_{max}, T_{min} and T_{mean} (at daily scale) time series at the Careser Diga, computed with reference to the observed values, were 0.69, 0.81, 0.90, and 0.92 respectively. These are relatively high values, ensuring that the values used for gap-filling the time series have a good (for precipitation) and an excellent (for the temperature) correspondence with the real (missing) data.

Possible sources of non-homogeneity in the time series are sensor replacements and location changes of the stations, both introducing bias in the measurements. Climate change is another source of non-homogeneity that should be identified and, contrary to the previous ones, retained and analyzed. The location of the stations remained unchanged since their installation and therefore sources of non-homogeneity may be either sensor replacement or climate change. We assume that non-homogeneity due to climate change is characterized by a change point followed by a trend, while sensor replacement is likely characterized by a shift, also starting from a change point. To identify such sources of non-homogeneity, the Pettitt test (Pettitt, 1979) was first applied to locate the change point, when present. Successively, the portion of the time series from the change point to the end was analyzed with the Mann Kendall (MK) test (Conover, 1999); the linear trend, evaluated with the following expression (Sen, 1968): $Q_{ij} = (z_j - z_i)/(j - i)$, for $j > i$, was then removed and the resulting detrended time series analyzed again. The Pettitt and Mann–Kendal tests were performed by using the python packages *pyHomogeneity* (Hussain, 2020) and *pyMannKendall* (Hussain, 2023; Hussain and Mahmud, 2019-07-25), respectively.

The Mann–Kendall test assumes that the time series values are uncorrelated and equally distributed. Unfortunately, these conditions are seldom fulfilled in geophysical and hydrological time series. For

this reason in the present work, the MK-test was used with caution, as described in Section 5, preferring to evaluate changes and tendencies utilizing moving averages, which smooth local variations, and the wavelets analysis discussed in Section 5. Therefore, the MK-test was used only to highlight the presence of a progressive change (trend), rather than an abrupt one, which is typical of sensor displacement or replacement.

4.5. Wavelet analysis

The Wavelets Transform (WT) was used to analyze the change in time of the dominating modes of variability of the flow rate at the Careser Baia gauging station. WT is a powerful tool, often used to disentangle the dominant scales of variability of non-stationary (in time) signals and identify their modes of variation (Torrence and Compo, 1998).

The continuous wavelet transform, $W_i(s)$, of a discrete signal $\{z_1, z_2, \ldots, z_n\}$, where s is the scale of variability, i is the time step index and n is the number of elements of the time series, is defined as the convolution of the signal z_i, $i = 1, \ldots, n$ with the wavelet function Ψ (Torrence and Compo, 1998):

$$W_i(s) = \sum_{i'=0}^{n-1} z_{i'} \Psi^* \left[\frac{(i' - i)\Delta t}{s} \right], \tag{2}$$

where Δt is the sampling time step and the superscript * indicates the complex conjugate. The wavelet function $\Psi(\eta) = (2\pi s/\Delta t)^{1/2} \Psi_0(\eta)$, $\eta = \frac{(i'-i)\Delta t}{s}$, is obtained by normalizing the "mother" wavelet function $\Psi_0(\eta)$. As mother wavelet, we used the Morlet function, widely employed in the analysis of geophysical signals and proven to be effective in detecting oscillations in time series (Torrence and Compo, 1998):

$$\Psi_0(\eta) = \pi^{-1/4} e^{\imath \omega_0 \eta} e^{-\eta^2/2} \tag{3}$$

where $\imath = \sqrt{-1}$ and according to Torrence and Compo (1998) ω_0 was set equal to 6.

The distribution of energy among the modes of variability (periods) is described by the wavelet power spectrum (WPS): $\sigma^2_W(i, s) = |W_i(s)|^2 = W_i(s)\, W_i^*(s)$. Relevant information on the nature of the signal can be obtained by analyzing how signal energy, which is proportional to the amplitude of the fluctuations, varies with time. This can be obtained by integrating the WPS over the investigated range of scales.

The continuous WT was applied to the daily reconstructed flowrate time series by using the python module *PyCWT* (Krieger et al., 2023) based on the routine developed by Torrence and Compo (1998).

5. Results

5.1. Homogeneity test

The Pettitt test was applied to the reconstructed (gap-filled with the modeled values) time series of the annual precipitation and the annual mean of the daily temperatures (T_{max}, T_{min} and T_{mean}) at the Careser Diga station. The analyzed time series are shown in Fig. 3 and the results of the test are summarized in Table 1. We evaluate the presence of a change point using the $p-$ value with a significance level of 95%. At this significance level, a value of $p \leq 0.05$ indicates that the deviation from the null hypothesis (the time series is homogeneous) is statistically significant and, as a consequence, the evidence is strong in favor of the presence of a change point (this is indicated with F in the second column of Table 1). On the other hand, when $p \geq 0.05$, the deviation from the null hypothesis is not significant, and therefore it cannot be rejected (this is evidenced by T in the second column of Table 1).

The total annual precipitation time series is homogeneous with no change points since the potential change point in 2008 is statistically not significant (as demonstrated by the p value of 0.35). On the contrary, change points were detected at the years 1991, 1994, and 1988 in the time series of T_{max}, T_{min} and T_{mean}, respectively. The Mann–Kendall test was then applied to the last portion of the temperature time series starting from the change point, obtaining the Sen's slope coefficients reported in the last column of Table 1, which were used to remove the trends. The resulting detrended time series are homogeneous as shown by the values of $p > 0.05$ reported in the last three rows of Table 1. An increasing trend is consistent with the effect of global warming, rather than other exogenous effects, which typically introduce a step change, and is consistent with observations at the global scale showing an increasing almost linear trend in the global temperature since the middle of 1980s (IPCC, 2023, Figure 2.1). Changing points vary according to the sensitivity of the variable to global warming with T_{max} showing the largest sensitivity, T_{min} the smallest, and T_{mean} intermediate.

Table 1
Pettitt test of homogeneity applied to the total annual precipitation (P) and the annual average of daily air temperatures (T_{max}, T_{min} and T_{mean}) at the Careser Diga meteorological station. The Null Hypothesis is that the time series is homogeneous and at 95% significance level a value of $p \leq 0.05$ indicates strong evidence in favor of the presence of a change point. For the temperatures, the test was repeated after detrending from the change point (CP) to the end of the time series with the Sen's slope sl (°C y^{-1}), and the results are shown in the last three rows.

Variable	Null Hyp.	CP	p	sl (°C y^{-1})
P	T	2008	0.35	–
T_{max}	F	1991	0.00	0.022
T_{min}	F	1994	0.00	0.052
T_{mean}	F	1988	0.00	0.046
T_{max} (detrended)	T	1960	0.19	–
T_{min} (detrended)	T	1971	0.37	–
T_{mean} (detrended)	T	1960	0.25	–

Table 2
Pettitt test of the monthly precipitation and the monthly average of the daily temperatures (T_{min}, T_{max} and T_{mean}). In bold are indicated the $p-$ values < 0.05, which identify statistically significant change points.

Month	Precipitation		T_{min}		T_{max}		T_{mean}	
	CP	p	CP	p	CP	p	CP	p
JAN	1969	0.09	1988	**0.01**	1988	**0.00**	1988	**0.00**
FEB	1966	0.65	1987	0.49	1989	**0.00**	1989	**0.04**
MAR	1954	0.48	1989	0.10	1989	**0.00**	1989	**0.00**
APR	1948	0.99	2002	**0.01**	1992	**0.00**	1995	**0.00**
MAY	1968	0.77	1993	**0.00**	1992	**0.00**	1992	**0.00**
JUN	2007	0.72	1993	**0.00**	1993	**0.00**	1993	**0.00**
JUL	1987	0.16	1982	**0.00**	1982	**0.00**	1982	**0.00**
AUG	1996	0.25	1988	**0.00**	1990	**0.00**	1990	**0.00**
SEP	1991	0.49	2009	0.43	1997	0.15	1997	0.29
OCT	1976	0.21	1967	0.08	1994	**0.01**	1983	**0.03**
NOV	1972	0.43	2001	0.08	1991	**0.02**	2001	**0.03**
DEC	1977	0.84	1970	0.07	1983	**0.00**	1970	**0.01**

The Pettitt test was also applied to the annual time series of the monthly precipitation and the monthly means of the daily temperatures with the results summarized in Table 2. In agreement with the previous analysis, the Pettitt test confirmed the absence of change points in the monthly precipitations, since all p values are larger than 0.05 (third column of the Table). On the other hand, change points were detected in the time series of T_{min} from April to August, and also in January, with stronger evidence (i.e., smaller p-values) in the summer months. For T_{max} change points were detected in all months, except September, and this shows that global warming has a more prominent effect on the maximum than on the minimum daily temperatures. This is reflected in the mean daily temperature, which also shows change points similar to T_{max}. Moreover, change points for the summer months were all located in the 1990s. The Pettitt test was repeated with the daily temperatures spatially averaged over the extension of the glacier in 1987 obtaining responses consistent with the analysis at the Careser Diga.

A similar analysis was conducted for the time series of glacier winter accumulation C_w (mm w.e.), summer ablation A_s (mm w.e.), net mass balance B_n (mm w.e.) and ablation volume V_A (m^3 w.e.), the latter

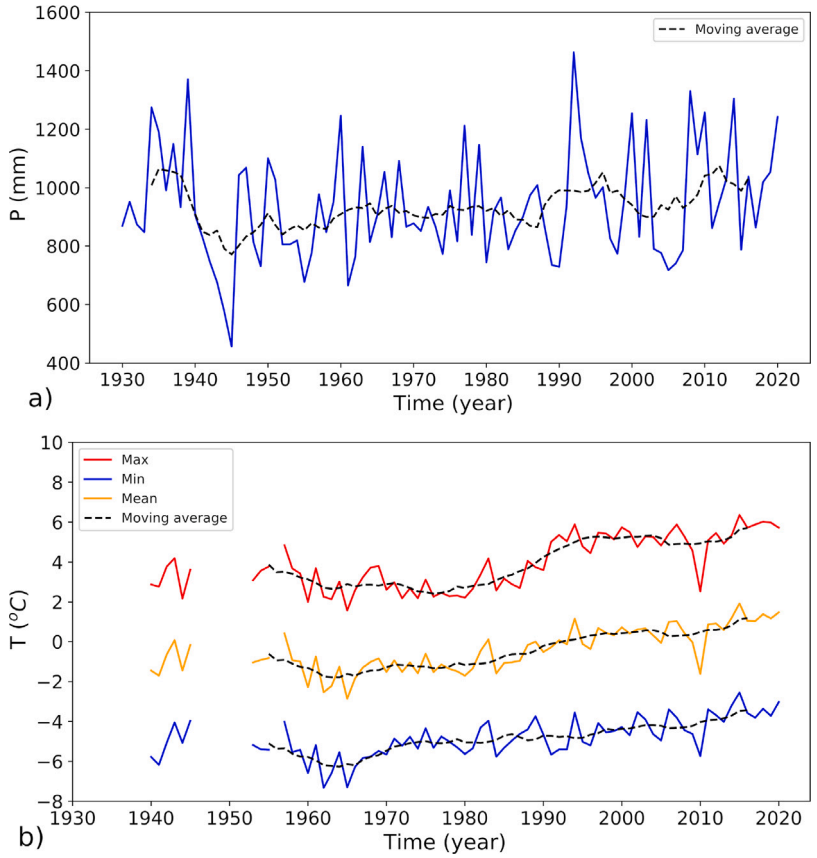

Fig. 3. Precipitations and temperatures at the Careser Diga meteorological station: (a) Total annual precipitation, (b) Annual average of the maximum, minimum, and mean daily temperatures. Dashed lines indicate the 9-year moving averages. Gaps in the time series were filled by KED using the measurements at a maximum of 32 neighboring stations, for precipitations since 1930 at the monthly time scale and for temperature since 1976 at the daily time scale.

Table 3
Pettitt test of the following glaciological variables: winter accumulation C_w, summer ablation A_s, net mass balance B_n and ablation volume V_A. The Null Hypothesis is that the time series is homogeneous and at 95% significance level a value of $p \leq 0.05$ indicates strong evidence in favor of the presence of a change point.

Variable	Null Hyp.	CP	p
C_w	T	1986	0.490
A_s	F	1998	0.000
B_n	F	1990	0.000
V_A	F	2008	0.001

computed as described in Section 4.1.2 and the others obtained from MeteoTrentino as described in Section 3.2 (Table 3). The time series of these variables are shown in Figs. 5a, 5b, 5d and 5c, respectively, with the dashed line representing the 9-year centered moving average. Notice that the moving average at a given time step was computed only when the time windows of 9 years contained more than 5 values.

In line with the precipitation at the Careser Diga station, the winter glacial accumulation time series is homogeneous ($p = 0.49 \gg 0.05$), while all the other quantities, including the ablation volume, show strong evidence of change points ($p < 0.05$). A change point in the net mass balance was identified in 1990, followed by a change point in summer ablation in 1998 and one in the ablation volume in 2008. Ablation is the dominant component of the summer runoff and it increases monotonously as an effect of global warming. However, runoff volume first increases up to the middle of the 1990s and then it decreases because of the progressive reduction of the glacier area which offsets the increase of ablation.

5.2. Impact of warming on glacier melting

Glacier runoff hinges on the interplay between the ablation and the hypsometric curve of the glacier area, both changing with time. As shown by Carturan et al. (2013b), the Careser Glacier is without accumulation area since the early 1980s, given that its ELA is above the highest glacier elevation, with only a few exceptions in the colder years (Carturan and Seppi, 2007; Baroni et al., 2017; Carturan et al., 2013b). The hypsometric curves of Figs. 4a and 4b show a reduction of the elevation range with time, which is accompanied by the increase of the glacier's minimum elevation of 98 m from 2856 m a.s.l. in 1958 to 2954 m a.s.l. in 2015, and a reduction of the maximum elevation of 37 m (see Table 4). The retreat is particularly evident after 2003 and in 2015 most of the glacier area was above 3000 m a.s.l. (the glacier was composed of a main unit, accounting for 77% of the total area, and other 5 smaller patches). This rapid retreat is in line with the global analysis conducted by Paul et al. (2004) and by Jiskoot and Mueller (2012) regarding glaciers of the upper Columbia River basin.

In accordance with the precipitation at the Careser Diga (Fig. 3a), no change points were detected in the winter accumulation, C_w, which shows stationary oscillations of wide amplitude around the 9-year moving average (Fig. 5a). These two signals are correlated with a Spearman rank correlation of $r = 0.58$, ($p = 0.0001$), which is satisfying considering the lower elevation of the meteorological station and the disturbing effect of measurement errors. In a recent study by Grossi et al. (2017) biases between 15% and 66% were observed in solid precipitations measured at rain gauges belonging to the same region. On the other hand, summer ablation A_s increased steadily with time (i.e., it became more negative) as shown in Fig. 5b, with smaller oscillations around the moving average with respect to C_w.

Table 4
Geometrical characteristics of the Careser Glacier. Per. indicates the perimeter of the glacier, Area is its area and Spec. Per. is the ratio between the perimeter and the area.
Source: The Equilibrium Limit Altitude (ELA) was extracted from Carturan and Seppi (2007) and Baroni et al. (2017).

Year	Per. (km)	Area (km^2)	Spec. Per. (km^{-1})	Mean Alt. (m a.s.l.)	Median Alt. (m a.s.l.)	Min Alt. (m a.s.l.)	Max Alt. (m a.s.l.)	ELA (ma.s.l.)
1958	24.7	4.88	5.07	3066	3070	2856	3316	–
1987	30.2	3.95	7.63	3064	3072	2858	3314	3485
2003	24.0	2.84	8.45	3063	3073	2860	3288	3700
2015	16.9	1.39	12.24	3086	3089	2954	3279	3280

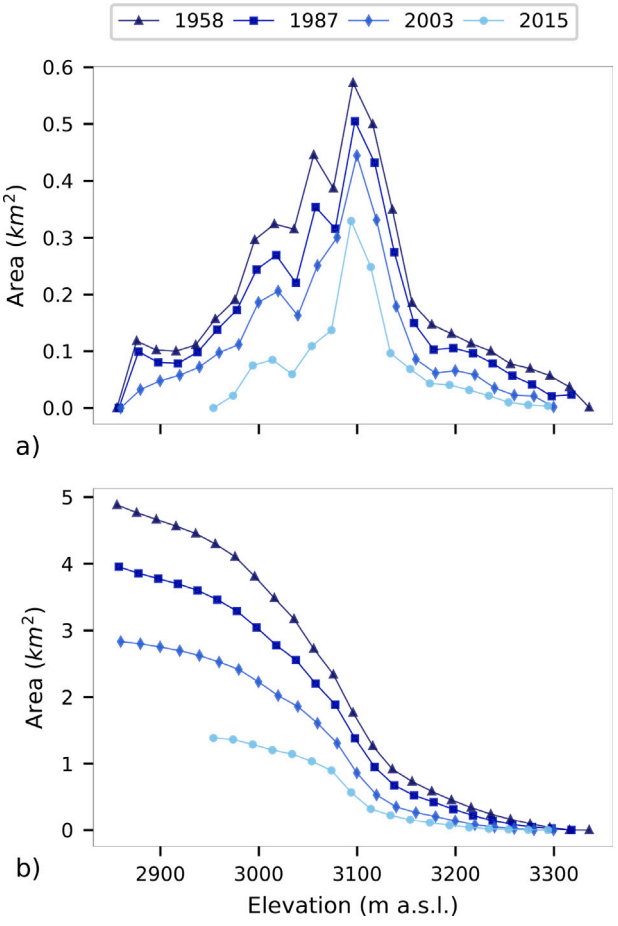

Fig. 4. (a) The portion of the glacier surface at different altitudes; (b) Glacier surface above a given elevation (Hypsometric curve) of the Careser Glacier.

The annual means of the spatially averaged air temperatures (with reference to the glacier area in 1987) are shown in Fig. 6 together with their 9−year moving average. The minimum temperature shows a small quasi-linear increase of the 9-year moving average from a minimum value of −7.1 °C in 1976 to a maximum value of −5.8 °C in 2020, corresponding to an increase of 1.2 °C in 45 years. The moving average of maximum daily temperature increased by 3.14 °C in 37 years, from 1980 to 2016, with two increasing trends, between 1980 and 1995 and between 2003 and 2016, and an intermediate period with a slight reduction. The moving average of the mean daily temperature increased from −4.11 °C in 1980 to −1.61 °C in 2016, with an overall increase of 2.5 °C in 37 years.

The impact of the observed rise of the air temperature on the ablation is better analyzed by considering its cumulative Degree-Days (DD) between May and September (153 days), corresponding to the conventional ablation period between the two successive topographic surveys used to compute the glacier mass balance. This cumulative temperature is a proxy of the energy that the glacier receives during ablation. Fig. 7 shows that DD increased between 1976 and 2020 with significant oscillations around the 9-year moving average, which increased as well from 198 °C in 1980 to 584 °C in 2016. In the same period, the mean temperature of the ablation period (i.e. $DD/153$) increased from 1.3 °C to 3.8 °C, i.e. 2.5 °C in 37 years, in agreement with what observed for the annual mean of the mean daily temperature.

The cause of the progressive increase of the ablation shown in Fig. 5b can be identified in the rise of temperature due to global warming as confirmed by the high Spearman rank correlation ($r = -0.74$, $p \sim 0$) between the time series of summer ablation and the summer cumulative temperature.

5.3. Glacier runoff

The modeled time series of the flow rate are compared in Figs. 8a and 8b with the observed ones at the daily and monthly time scales, respectively. The good agreement between the measured and modeled streamflow, suggested by the relatively high NS values at both the daily ($NS = 0.69$) and monthly ($NS = 0.89$) temporal scales, is confirmed by visual inspection of the figures. The second column of Figs. 8a and 8b show the scatter plots of the modeled against the measured stream flow at the daily and monthly time scales, respectively. Fig. 9 shows the corresponding summer (May-October) mean streamflow and its 9-year moving average.

The mean flow rate oscillates around the 9-year moving average, which first increased from 1.56 $m^3 s^{-1}$ in 1979 to 1.96 $m^3 s^{-1}$ in 1993, and successively declined to 1.20 $m^3 s^{-1}$ in 2019, resulting in an average loss rate of 0.03 $m^3 s^{-1} y^{-1}$. This pattern agrees with the glacier behavior discussed in Section 5.2 with the streamflow that mirrors the summer ablation volume V_A. Both streamflow and V_A (Fig. 5c) show a tilting point in the middle of the 1990s while the ablation increases (i.e., its absolute value increases) at a constant pace (Fig. 5b).

We conducted the wavelets analysis to investigate non-stationary (in time) dynamics of the streamflow signal. Since this analysis requires a continuous time series, we assumed zero streamflow in the winter period, from November to April. The wavelet power spectrum $\sigma^2_W(i,s)$ of the daily flow rate, obtained by using the Morlet base wavelets transform (Torrence and Webster, 1998), is shown in Fig. 10b as a function of time, indicated by the time step i, and scale of variability, s (period), with a log_2 color scale. As expected, $\sigma^2_W(i,s)$, $i = 1, \ldots, n$ peaks at the period of 1 year, as a consequence of the remarkable seasonality of streamflow (Fig. 10c). No significant attenuation of this peak, as well as of the energy content in the interval 90–730 days (i.e., 3–24 months) represented by the mean variance $\overline{\sigma}^2_W(i) = \int_{s_1}^{s_2} |W_i(s)|^2 d\,s/(s_2 - s_1)$ with $s_1 = 90$ and $s_2 = 730$ days, are observed in Figs. 10b and 10d. However, the Pettitt test applied to the mean variance signal of Fig. 10d identified a change point in 1995 ($p = 0.0$) and an additional one in 2018 ($p = 0.0$), the latter refers to the detrended time series. The former change point coincides with the tilting point of the mean summer runoff shown in Fig. 9. The Sen's slope was $sl = -3.67 \times 10^{-6}$ $m^6 s^{-2} d^{-1}$ after 1995 and was not computed after 2018 because within the cone of influence and with only two years of data (2018–2019). The energy contained in the periods 3–24 months (Fig. 10d) decreased only slightly

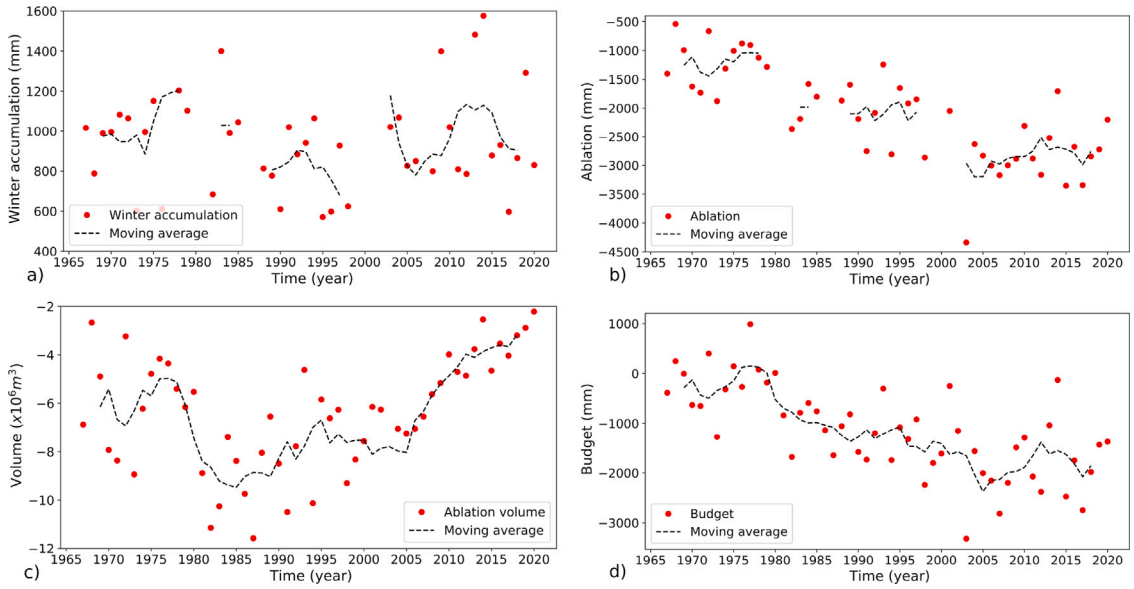

Fig. 5. Time evolution of the Careser Glacier; (a) winter accumulation C_w (mm w.e.), (b) summer ablation A_s (mm w.e.), (c) summer ablation volume V_A (10^{-6} m^3 w.e.), and (d) net mass balance B_n (mm w.e.). Dashed lines show the 9-year moving average computed with a centered window. The moving average is not computed when less than 5 values fall within the searching window.

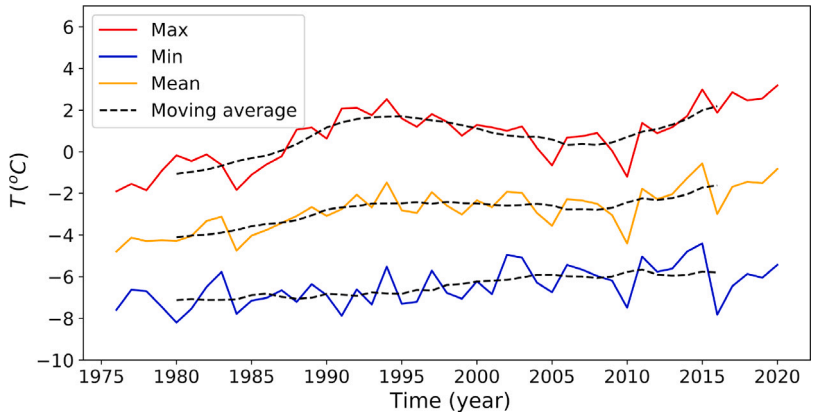

Fig. 6. Annual average of the spatially averaged maximum, minimum, and mean daily temperatures at the Careser Glacier with their 9-year moving average. The spatial average is computed with reference to the glacier surface area in the year 1987 by using KED with a maximum of 32 neighboring meteorological stations at elevation larger than 1000 m a.s.l.

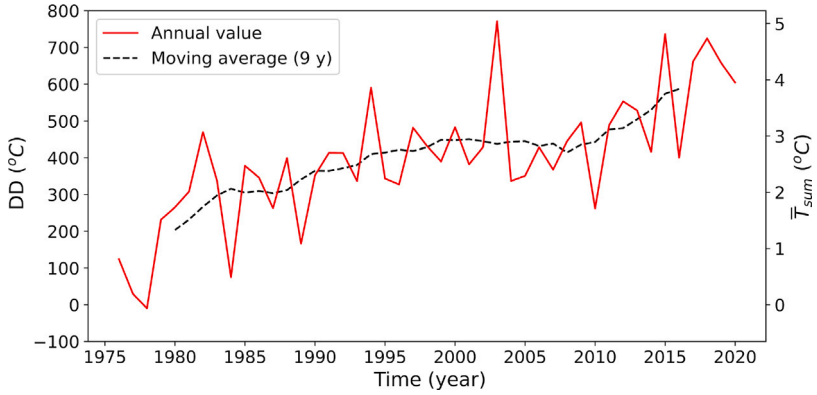

Fig. 7. Evolution of the cumulative daily mean temperature in the ablation period (153 days from May to September) at the Careser Glacier. The secondary axis shows the mean temperature over the same period: $DD/153$.

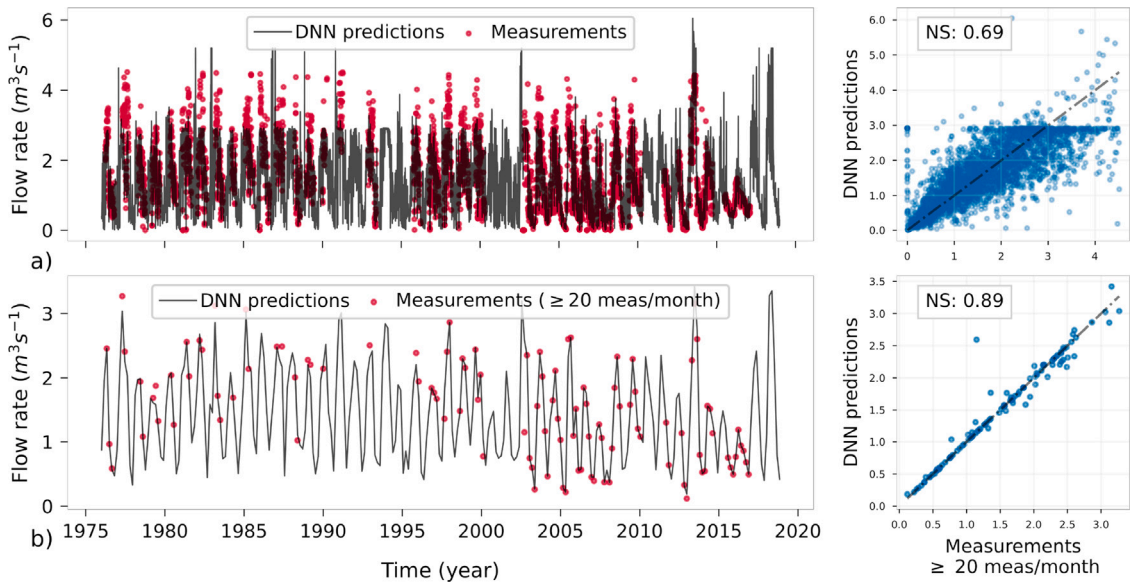

Fig. 8. Time series of the streamflow at the Careser Baia gauging station at the (a) daily and (b) monthly time scales. Computed and measured flow rates are represented by the solid line and the red dots, respectively. The monthly mean of the observed flow rate is computed only for months with more than 20 daily data available. (For interpretation of the references to color in this figure legend, the reader is referred to the web version of this article.)

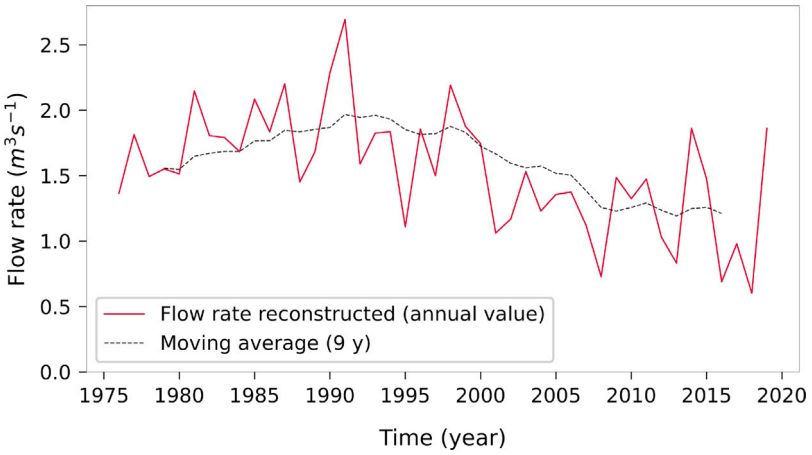

Fig. 9. Time evolution of the mean flow rate during the ablation period (May–October) at the Careser Baia gauging station, with the dashed line showing the 9-year moving average. Gaps in the original daily time series were filled with the DNN model.

with time, thereby suggesting that the observed reduction of the flow rate (Fig. 9) occurred in similar proportion in the summer season.

The assumption of zero winter streamflow (from November to April) was a somewhat obligated choice because of the lack of data. However, measurements performed in 2018 in a small tributary of the Careser Stream showed that the water temperature was always above freezing (see Figure S1 of the Supplementary Material and Figure 2 in Lencioni et al. (2022) for the CR1bis water temperature data), thereby suggesting the presence of running water. To highlight possible spurious effects introduced by the zero streamflow assumption, we repeated the wavelets analysis with the winter values provided by the DNN model. No significant differences are observed in the wavelets spectrum of the time series, as can be noticed by comparing Figs. 10b-d with Figures S2b-d of the Supplementary Material. The small to negligible differences observed in the spectra of the two signals suggest that for the purpose of our analysis both lead to the same conclusions.

To further investigate the observed reduction of the flow rate we reported in Fig. 11 the average monthly flow rate, for the ablation season, evaluated at 10-year intervals starting from the period 1976–1985 and ending with the period 2016–2019. The color-shadowed areas represent the interquartiles (i.e., the 50% interval of confidence). The seasonal peak decreases, particularly after the period 1986–1995, but the same happens for the flow rate from August to October, and these changes occurred in a way that preserved the amplitude of the seasonal oscillation. This is in line with what was already observed with the wavelets analysis. However an important change occurred after 2000: a progressive increase of the early summer runoff (from May to June), which is accompanied by the reduction of the peak in July, thereby suggesting an earlier start of the snow-melting season, which in turn is in line with the increase of the summer ablation shown in Fig. 5b. Furthermore, interannual variations increased with time as shown by the progressive widening of the interquartile range (the shadowed areas in Fig. 11).

Fig. 12, shows the monthly fraction of the total summer runoff as a function of time. The result of the Mann–Kendall analysis is reported in Table 5 and the dashed lines show the Sen's slope of the statistically significant linear trend evaluated between 1976 and 2019. Consistently with the previous analysis, statistically significant trends are observed in June (increasing), in August, and in September (both decreasing). The other months showed increasing trends, except October, but all

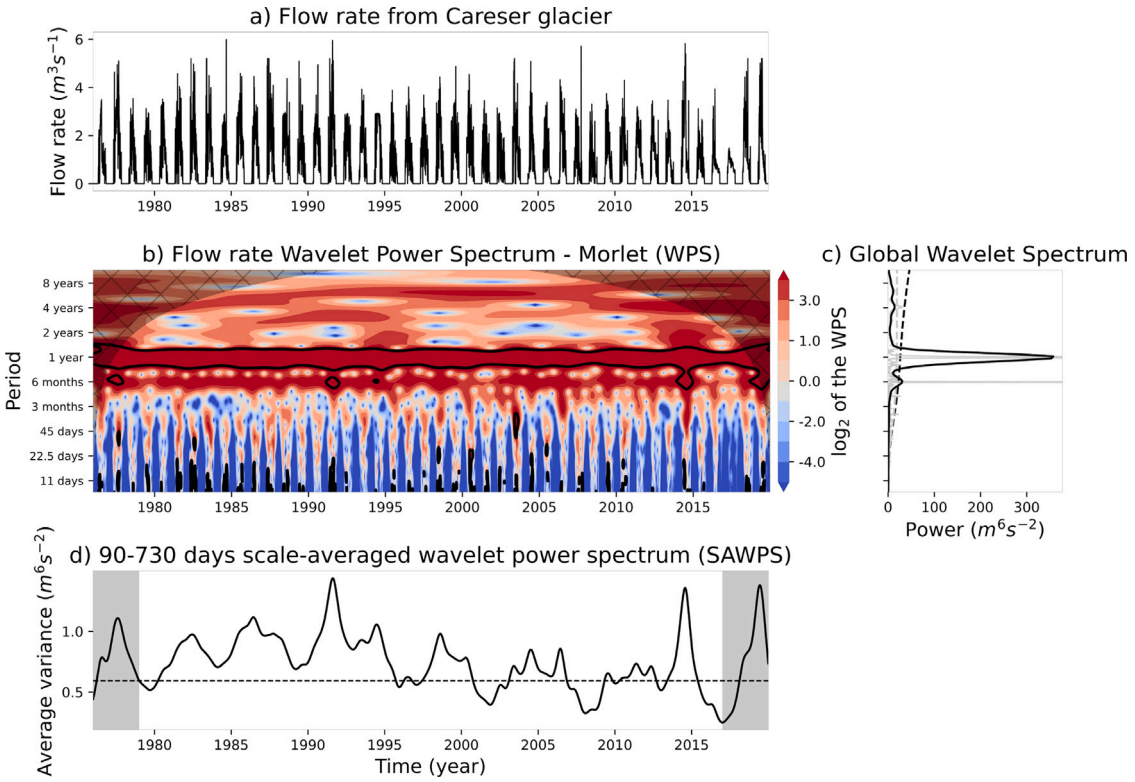

Fig. 10. (a) Time series of the flow rate at the Careser Baia gauging station; (b) Morlet-base Wavelet power spectrum; (c) Global power spectrum and d) 90–730 days scale-averaged wavelets power spectrum. The shadowed areas indicate the cone of influence.

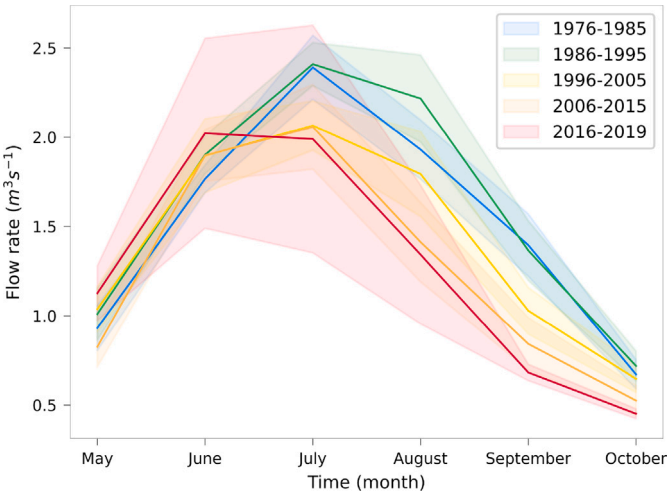

Fig. 11. Mean and interval of confidence (interquartile identified by the shadowed area) of the monthly flow rate at the Careser Baia for 10-year periods from 1976 to 2019. The last period is of 4 years (2016–2019).

are statistically not significant and therefore were not reported in the figure. The tendency of an earlier start of the ablation season, already observed in Fig. 11, is therefore confirmed by the rise of the fraction of summer runoff occurring in June. In agreement with this behavior, the amount of solid precipitation in May and June decreases with time, while the liquid fraction increases. This is shown in Fig. 13, which includes also the projected precipitations according to the selected climate models and the RCP 4.5 future scenario that will be discussed in Section 5.4.

Table 5
Mann-Kendall test of the monthly flow rate fraction. The null hypothesis is that the series has no trend, therefore a statistically significant trend is characterized by p values smaller than 0.05.

Month	Type of trend	Null Hyp.	slope y^{-1}	p [−]
May	no trend	T	0.088	0.127
June	increasing	F	0.178	0.002
July	no trend	T	0.003	0.927
August	decreasing	F	−0.113	0.019
September	decreasing	F	−0.151	0.004
October	no trend	T	−0.020	0.606

5.4. Future projections

The possible future evolution of the Careser Glacier and the associated streamflow is investigated here by using the EURO-CORDEX ensemble climate models with the future scenario RCP 4.5. The scenario RCP 8.5 produced similar results, after bias correction of temperature and precipitation, and therefore it is included in the Supplementary Material (Figures S3 and S4) and not analyzed here.

Temperature and precipitation projected by the climate models for the period 2020–2070 were bias corrected by the Quantile Mapping method (successfully employed for corrections of climate models by Dobler and Ahrens, 2008; Jakob Themeßl et al., 2011; Piani et al., 2010, for instance). The precipitation was separated between liquid and solid by assuming 0 °C as a threshold. The annual time series of the monthly precipitation partitioned into solid and liquid are shown in Fig. 13, where the vertical dashed line separates the observations from the projections. The progressive shifting of the precipitation from solid to liquid, already observed in the first two decades of this century is confirmed with a further reduction of the solid in favor of the liquid precipitation, though the variability among the climate models is large, as shown by the wide interquartile range.

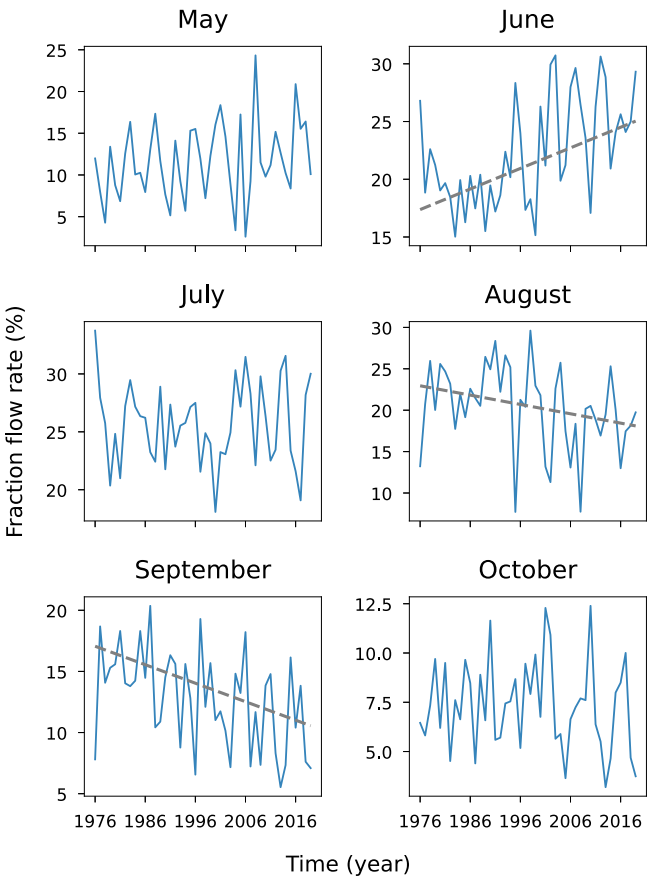

Fig. 12. Monthly relative contribution to the total runoff at the Caraser Baia. Dashed lines indicate the Sen's linear trend when the Mann–Kendall test identified a statistically significant trend.

The Mann–Kendall test confirmed the increase of the liquid precipitation in the summer months (from April to October, except September in which the trend is not statistically significant) and a contemporaneous reduction of the solid precipitation.

The DNN model was run with the meteorological signals of the climate models and the three models of future ablation presented in Section 4.2. The results are shown in Fig. 14. The shadowed areas indicate the interquartile of the eight EURO-CORDEX climatic models.

In all cases, the area occupied by the glacier shrinks with time, projecting the glacier to disappear in 2041 when the ablation is computed with the regression curve and in 2038 and 2045 when it is augmented or, respectively, reduced by the standard deviation. The interquartile range is small in all three cases.

Larger differences are observed for the projections of the flow rate and of the respective interquartiles. A general reduction of the flow rate, with wide oscillations, is confirmed also for the future projections with the catchment shifting progressively to the nival regime. In the projections, solid precipitations are no longer observed in July and August and are strongly diminished, almost disappearing, in June and September. A remarkable increase in liquid precipitation is observed in May and October, accompanied by a decline in solid precipitation. In addition, more rainfall occurs in April and November, confirming the stigmata of climate change already evident in the last decade.

6. Discussion

The comparative analysis of available and reconstructed meteorological, glaciological, and hydrological data at the Careser Glacier allowed us to identify the two main mechanisms controlling the observed hydrological changes: a remarkable increase of glacier ablation, driven by the increase of the temperature, that caused the rapid reduction of the glacier volume with an effect on streamflow that was offset by the concomitant decline of the glacier area.

The reduction of the glacier volume, widely reported in literature (Zanon, 1992; Carturan and Seppi, 2007; Carturan et al., 2013a,b) is shown to be driven by the increase of summer ablation (Fig. 5b), which occurs without appreciable changes in winter accumulation (see the 9-year moving average in Fig. 5b). This is in agreement with the analyses of the climatic drivers, in particular with the increase of the cumulative temperature in the ablation season (Fig. 7), and with the precipitation at the Careser Diga without changing points and with an almost constant moving average over the entire observation period (1976–2020), as shown in Fig. 3a. The lack of correlation between streamflow and precipitation during the ablation period (Spearman's rank correlation $r = 0.07$), and the significant correlation with minimum and maximum daily air temperature ($r = 0.54$ and $r = 0.52$, respectively) reinforce these conclusions. The increase of the air temperature drove the increase of ablation shown in Fig. 5b, which is offset by the reduction of the glacier area (Fig. 4), thereby leading to the reduction of the summer runoff volume starting from 1996 (Fig. 9). Moreover, a progressive increase of the liquid precipitation at the expense of the solid precipitation was observed in the spring (from April to June) and in October, with no appreciable changes in the accumulation period (November–March), when the precipitation was predominantly solid, and in summer (July–September) when liquid precipitation dominates. The distinct fractions of precipitation showed a higher correlation with streamflow (with Spearman's coefficients of $r = 0.34$ for the liquid fraction and $r = 0.31$ for the solid fraction), suggesting again the main role of air temperature in this process. These correlations between climatic factors and streamflow can be ascribed to the substantial impact of air temperature on both the melting process and the partitioning between liquid and solid precipitations, thus assuming a pivotal role in regulating the flow rate. The prominence of air temperature in this context may be further accentuated due to the southern exposure of the Careser Glacier, which results more exposed to the increase of the radiation, as supported by findings of other studies (Paul and Haeberli, 2008). Climate models indicate significant changes in the partitioning between solid and liquid precipitations. June and September, which currently are months with a significant amount of snowfall (though to a lesser extent with respect to the previous decades), are dominated by rainfall in the climate projections. Moreover, in October, the share of rainfall increases at the expense of snowfall, which decreases. All these changes indicate a shorter accumulation period accompanied by the rise of air temperature, which leads to higher ablation (Fig. 13).

These changes, which are all in the direction of shifting the Careser catchment from a glacio-nival to a purely nival regime, have profound effects on both the timing of runoff and its annual volume. Starting from the beginning of the systematic streamflow observations in 1976, the summer runoff volume first increased, due to the rise of temperature, reached a maximum in the middle of the 1990s, and then decreased at a constant pace in the following years. This behavior was already observed in other Alpine glacial environments (see e.g., Huss, 2011; Huss and Hock, 2018; Farinotti et al., 2012) and climate projections confirmed this tendency, with the catchment that is projected to complete the shift from the glacio-nival to the nival regime in the next 20 years.

The streamflow timing changed, with runoff that increased in the early summer months, driven by the rise of the temperature and the accompanying increase of the fraction of liquid precipitation, but diminished in the following months driven by the reduction of the ablation volume, with the larger fraction of liquid precipitation that was not enough to compensate for the loss. The peak discharge timing receded by about 5 days per decade from the reference period 1990 ÷

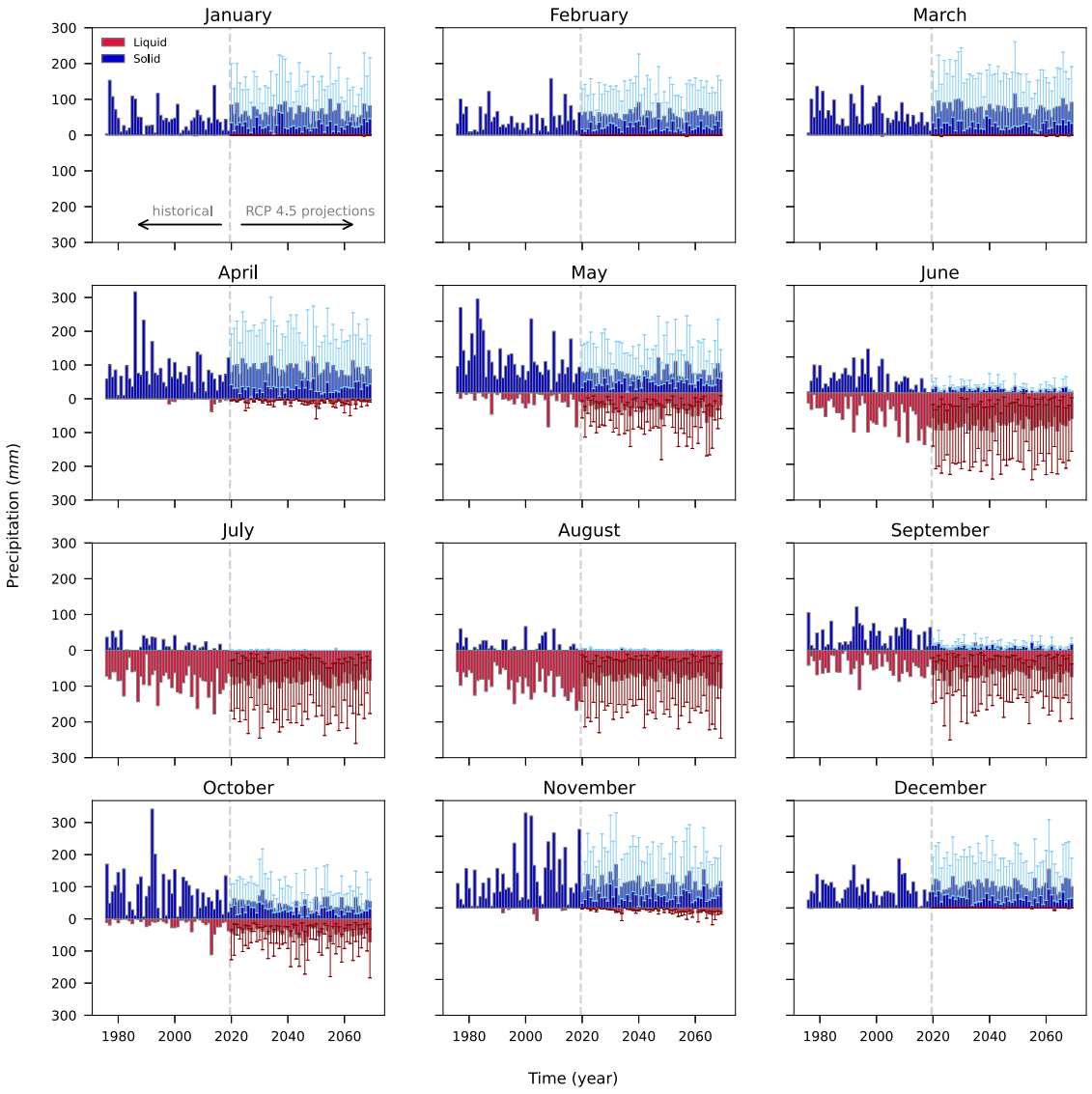

Fig. 13. Annual time series of the monthly precipitation partitioned between solid and liquid for the periods 1976–2019 and 2020–2070, the latter extracted from the eight EURO-CORDEX RCP 4.5 climate models used in the present work and bias-corrected as described in Section 4.2. The bars represent the mean and the whiskers the interquartile range. The vertical dashed line separates the measurements from the climate projections.

2000, in line with Farinotti et al. (2012) which reported a rate of 4.4±1.7 days per decade for nine Swiss catchments. In relative terms, runoff increased in June and decreased in August and September, while in the other months, the observed trends are statistically not significant in the observational period. Similar monthly statistical trends were observed in the European Alps by Huss and Hock (2018), who performed a global evaluation of the hydrological response to the mass loss of the Alpine glaciers.

Key to the above analysis was the reconstruction of the missing data in the streamflow time series with the DNN algorithm, which differently from conceptual or physically based models does not require the definition of the model's structure and the number of parameters (including their spatial and temporal variability) since the system functioning is learned from the data. This characteristic allows us to unveil complex and nonlinear relationships between external forcing and observational data, which may only be partially achieved with a model structure based on the modeler's knowledge and experience (Goodfellow et al., 2016; Shen, 2018). Bayesian model averaging (see e.g., Diks and Vrugt, 2010) or Bayesian model selection (see e.g., Höge et al., 2019) may be used to inform model structure with the available data, but this approach is less flexible than ML because constrained to the selected model structures. In other words, they do not allow to capture processes not envisioned in the models, though reflected in the data. On the other hand, the main limitation of ML methods is that their capability to identify system functioning depends on the amount of available data. Therefore, if less data are available than the minimum needed to identify the system functioning, conceptual or physically based methods are expected to provide a better prediction. Despite the high number of gaps in the daily time series, the available streamflow data was sufficient to infer system functioning and its temporal changes, as proven by the good agreement achieved in the training and validation sets (see Appendix B for a detailed explanation). With the DNN model, we captured the relevant relationships between drivers and streamflow, which provided a satisfactory reconstruction of the streamflow time series from 1976 to 2021. This is proven by the performance achieved, with NS reaching 0.69 and 0.89 at the daily and monthly scales respectively, and the good agreement between training, test and validation sets. For these reasons, we believe the same approach could offer valuable insights in similar situations.

In terms of performance, the accuracy of the DNN model prediction is higher than that commonly accepted in other modeling studies using conceptual or process-based models. For example, Compagno et al.

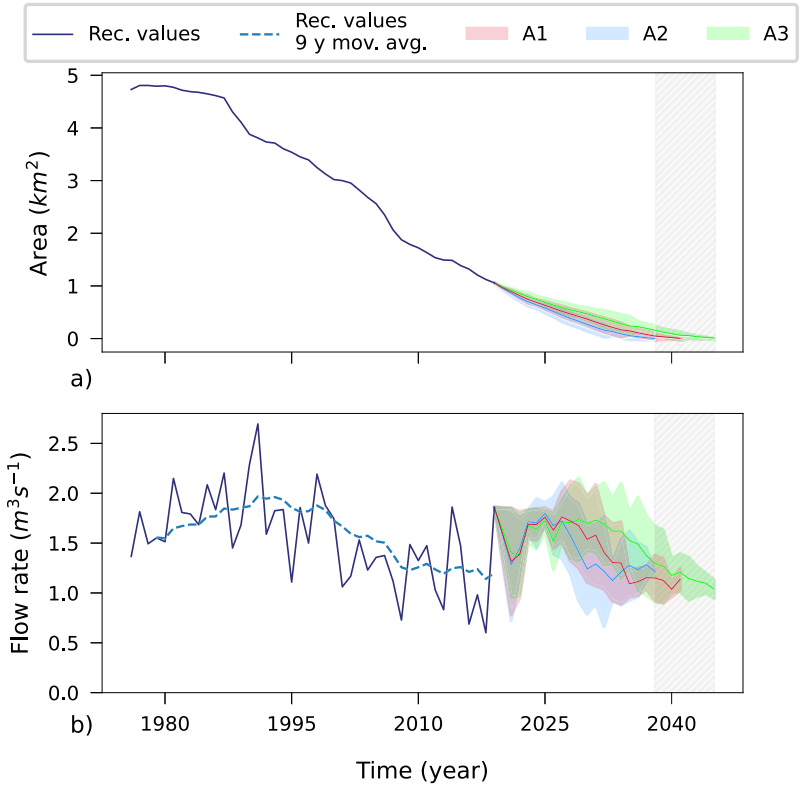

Fig. 14. Evolution of glacier area, (a) and summer mean flow rate, (b) at the Careser Baia in the period 1976–2019 and for the future scenario RCP 4.5. The following three cases are shown: the summer ablation estimated by linear regression with the mean air temperature (scenario A_1, red curve) and augmented (scenario A_2, blue curve) and reduced (scenario A_3, green curve) by the standard deviation. These three cases are presented in Section 4.2. The shadowed area represents the variability between the eight EURO-CORDEX models used in the present work. (For interpretation of the references to color in this figure legend, the reader is referred to the web version of this article.)

(2021) presented the results of the application of the GloGEMflow model (Huss and Hock, 2015; Zekollari et al., 2019) to 3927 glaciers in the Alps, obtaining, for the annual mass balance, a mean squared correlation coefficient as low as $r^2 = 0.29$, which increases to $r^2 = 0.52$ with data aggregated to elevation bands. Another example of the better performance achieved by the DNN compared to a process-based model (SWAT) was presented by Rahman et al. (2022), which compared the two approaches for the simulation of streamflow in different subbasins in the Upper Indus Basin. They claimed that the reason for the poor performance of SWAT might be in the choice of the parameters, the approximations introduced for the physical processes represented, and the inability of SWAT to detect the peaks of the streamflow. With DNN they achieved Nash–Sutcliffe values close to 0.9, while SWAT provided much lower values close to 0.7.

The future evolution of the Careser Glacier was also investigated by Carturan et al. (2013a), assuming unchanged climatic conditions. They have foreseen a progressive reduction of the glacier surface (0.65 km^2 in 2020, 0.15 km^2 in 2040) with the complete disappearance within 2060. In our work, the averaged value of the area was 0.97 km^2 in 2020, while the climatic projections (for the scenarios of ablation A1, A2, and A3), led to a faster vanishing of the glacier with an averaged area of 0.15 km^2 reached already in 2035 and of 0.07 km^2 in 2040. We depicted a more dramatic scenario, likely as a result of an acceleration of climate change effects.

In Carturan et al. (2019), data from hydrometric gauging stations in the upper part of the Noce River catchment were analyzed, including one site close to Careser dam (Pian Venezia). The Noce River originates from the confluence of the Careser Stream into the Noce Bianco downstream of the Careser dam, Fig. 1. Our findings are in agreement with this work, which showed a shifting of the runoff peak from mid- to early summer in the 2000s (from August to July) with a progressive transition from the glacial to the nival regime. These effects are more evident at the Careser Glacier, with the current peak of streamflow in June. This could be attributed to its south-facing orientation and the amplifying effect of its diminishing volume.

In summer, the glacier is an important source of water for the downstream freshwater ecosystems, for a cascade of four hydropower systems, and ensures suitable conditions for canoe and rafting, at the professional level, further downstream. In addition, the reduction of summer streamflow, together with the increase in air temperature has been the driving force of the remarkable rise of water temperature in the Careser Stream, immediately downstream of the glacier. The impact of the changes in the hydrological regime so far experienced by the Careser Stream on the freshwater ecosystem was investigated by Lencioni et al. (2022). The conclusions from Lencioni et al. (2022) and the projections presented here indicate in a relatively near future the shift of this freshwater environment to conditions more favorable for species adapted to a warmer climate. In addition, the reduction of the summer streamflow projected in the coming years will cause a reduction of hydropower production in the same season, at least partially compensated by a foreseen increase in spring production due to the anticipation of the ablation period. However, the optimal use of the Careser reservoir may contribute to mitigate these changes.

7. Conclusions

We studied streamflow changes of the Careser Stream, a glacial headwater of the Adige River, in northeastern Italy. The Careser Glacier, which feeds the stream, losses mass since the early 1970s but in the last two decades the rate of shrinking increased dramatically causing remarkable changes in the annual runoff and seasonal streamflow timing. Hydro-climatic changes driving this behavior were detected by performing a comprehensive analysis of precipitation, temperature, flow rate, and glacier mass balance. Successively, the impact of these

changes on the hydrological system, composed of the glacier and the non-glacial portion of the catchment, was analyzed by considering the recorded time series of the glacier budget and streamflow measured at the Careser Baia gauging station, immediately upstream of the Careser reservoir with a total contributing area of $8.5\,km^2$. In the early 1970s, slightly over half of this area was covered by the glacier, which experienced a dramatic reduction in size over the years. Precipitation, temperatures, and streamflow measurements were supplemented with geostatistical (for precipitation and temperature) and machine learning (for streamflow) modeling to reconstruct missing information at the glacier and the outlet of the investigated catchment.

We found that streamflow alterations were caused chiefly by the increase in the air temperature in the summer months and the progressive increase of the fraction of liquid precipitation at the expense of the solid fraction in the same months. At the glacier, the cumulative summer air temperature, between May and September, increased since the early 1970s with the 9-year moving average that increased as well with a rate of $14.85\,°C\,y^{-1}$ from $198\,°C$ (seasonal mean of $1.3\,°C$) in 1980 to $584\,°C\,day$ (seasonal mean of $3.8\,°C$) in 2016. On the other hand, both winter snow accumulation and winter precipitation, the latter evaluated at the Careser Diga, were stationary over the entire observational period. As an effect of the remarkable increase in the air temperature, summer ablation increased dramatically resulting in the rapid shrinking of the glacier. This was accompanied by the increase of the liquid precipitation in spring and autumn chiefly at the expense of a reduction of the solid precipitation. From a hydrological point of view, the Careser system experienced an increase in the summer ablation, which produced first a moderate increase of streamflow until the middle of the 1990s, when the reduction of the glacier area offsets the increase of summer ablation leading to a decline of the streamflow, slightly mitigated by the increase of the liquid precipitation, after the peak reached in 1996. As a consequence of these changes, in the last two decades, the catchment shifted progressively from the glacial to the nival regime, and the investigated climate models project to complete this transition within 2040.

CRediT authorship contribution statement

Maria Grazia Zanoni: Software, Formal analysis, Writing – original draft, Writing – review & editing. **Elisa Stella:** Formal analysis, Writing – original draft, Data curation. **Alberto Bellin:** Supervision, Conceptualization, Methodology, Software, Formal analysis, Editing, Reviewing.

Declaration of competing interest

The authors declare that they have no known competing financial interests or personal relationships that could have appeared to influence the work reported in this paper.

Data availability

The model output data generated with the DNN model and the future projections have been deposited in CSV format in a Mendeley Data repository under accession code Creative Commons Attribution 4.0 International. Mendeley Data: https://data.mendeley.com/datasets/z4b439psmn/1.

Acknowledgments

The authors acknowledge funding by the Italian Ministry of Education, University and Research (MIUR) within the frame of the Departments of Excellence Initiative 2018–2022 attributed to DICAM of the University of Trento. The authors are also indebted to Meteotrentino (www.meteotrentino.it for providing the meteorological, streamflow, and glacier mass balance data used in the present work and Weather South Tyrol (https://meteo.provincia.bz.it) for providing the data of the meteorological stations of the Autonomous Province of Bolzano. The authors thank also Michael Christian Matiu (University of Trento) for his collaboration in the extraction of the climate projections from EURO-CORDEX ensemble models. Special thanks to Oscar Cainelli and Erica Meneghetti for data collection and preliminary analyses not included in the present work and to Tiziano Martinelli for providing the water stage data we used to elaborate the rating curve of the Careser Baia gauging station.

Appendix A. Kriging with external drift

According to the general geostatistical model of spatial variability the unknown value of the Random Space Function (RSF) $z_i(\mathbf{x})$ at the location $\mathbf{x}$ and time step i can be estimated as follows:

$$z_i^*(\mathbf{x}) = \sum_{j=1}^{n_i} \chi_{j,i}(\mathbf{x}) z_{j,i}, \quad i = 1, \ldots, n. \tag{A.1}$$

where $\chi_{j,i}$, $j = 1, \ldots, n_i$ are the kriging weights and $z_{j,i}$ are the observed values at the n_i active meteorological stations involved in the estimation. Notice that the stations included in the linear combination of Eq. (A.1) may change with the time step i, thereby leading to a different set of weights. In other words the weights $\chi_{j,i}$ depend on both the point of estimation and the time step. The KED algorithm assumes that the mean of the SRF z is spatially variable and depends linearly from a secondary variable, chosen here to be the elevation h, which therefore enters in the system of equations of the weights $\chi_{j,i}$ (see Goovaerts et al., 1997, ch. 6.1.3 for an exhaustive explanation).

The following exponential covariance function was used to characterize the RSF z:

$$C(r_1, r_2) = \begin{cases} \sigma^2 e^{-r'}, & \text{for } r > 0 \\ \sigma_0^2 + \sigma^2, & \text{for } r = 0 \end{cases} \tag{A.2}$$

where, $r' = \sqrt{\frac{r_1^2}{\lambda_1^2} + \frac{r_2^2}{\lambda_2^2}}$ and r_i, $i = 1, 2$ is the ith component of the two-point separation distance with λ_i being the correlation length along the same direction. In addition, σ^2 is the variance and σ_0^2 is the nugget effect, which takes into account the variability occurring at spatial scales smaller than those resolved by the measurements. To reduce the number of parameters, the covariance function (A.2) was assumed isotropic, i.e. $\lambda_1 = \lambda_2 = \lambda$.

The model (A.1) requires for its application the identification of the three model's covariance parameters (λ, σ_0^2 and σ^2) and two hyper-parameters. The first hyper-parameter is the maximum number, n_{max}, of stations used in Eq. (A.1) and chosen with the nearest neighborhood criteria among those at elevation larger than $h_{z,lim}$, which is, therefore, the second hyper-parameter. This choice is performed by minimizing the following objective function:

$$RMSE = \frac{1}{n} \sum_{i=1}^{n} \left[z_i^* - z_i \right]^2 \tag{A.3}$$

evaluated at the Careser Diga station (station T0065), which was then excluded from the set of n_{max} stations used in Eq. (A.1). In Eq. (A.3) z_i is the observed variable at the Careser Diga station at time step i, since the beginning of the observations, and z_i^* is the corresponding modeled (kridged) value. To simplify the optimization procedure several combinations of hyper-parameters were pre-selected and the RMSE was minimized for each of them by searching the space of the covariance parameters using the particle swarming algorithm (Eberhart and Kennedy, 1995; Castagna and Bellin, 2009). The combination of hyper-parameters that produced the global minimum (i.e. the minimum of the sum of the optimal (minimum) RMSE of T_{min}, T_{max} and T_{mean}) was $n_{max} = 32$ and $h_{z,lim} = 1000\,m$ a.s.l., and they were used in a final search of the covariance parameters space providing the optimal parameters for each variable.

Table A.6
Optimized parameters of the covariance function (A.2), minimum $n_{i,min}$ and maximum $n_{i,max}$ number of stations used in the interpolation.

Variable	σ_0^2 [°C]^2 or [mm]^2	σ^2 [°C]^2 or [mm]^2	λ [km]	$n_{i,min} - n_{i,max}$ [–]
P	49.98	19.55	6.98	10 – 24
T_{min}	1.78	18.05	2.94	5 – 23
T_{max}	39.02	16.26	5.61	5 – 23
T_{mean}	10.92	36.81	3.47	5 – 23

Table A.6 shows the optimal parameters of the covariance function, the minimum ($n_{i,min}$), and the maximum ($n_{i,max}$) number of stations used in the models.

The above optimization procedure was repeated for the precipitation aggregated at the monthly scale verifying that the same set of hyper-parameters was optimal also in this case. Notice that KED was applied to the precipitation aggregated at the monthly scale because the model (A.1) cannot handle intermittency, which characterizes precipitations at the daily and smaller time scales. The meteorological stations lacking the measured value at the time step i were excluded from the sum in Eq. (A.1), thereby n_i changed with the time step i, such as the weights $\chi_{j,i}$, and was limited to a maximum value of $n_{max} = 32$, when all the 32 meteorological stations selected with the nearest neighborhood criteria were active.

Appendix B. Dense deep feed-forward neural network

Streamflow was modeled from 1976 to 2019 by using the Dense Deep feed-forward Neural Network (DNN) algorithm with dense and unidirectional connections between the neurons of the hidden layers. The model was built by training and validating the DNN algorithm with the available summer streamflow measurements.

The DNN model was developed as follows. The streamflow time series, in the summer period, was randomly partitioned into training and test sets, containing 80% and 20% of the data, respectively. Considering the relatively low amount of data, with respect to the typical Machine Learning (ML) application, the validation step was performed directly on the training set with the k-fold cross-validation procedure as suggested by Raschka (2015). Accordingly, the training set was subdivided into $k = 10$ groups, and in turn, each one of them was used as the test set, with the remaining $k - 1 = 9$ groups assuming the role of the training set, on which the model was trained. For a given choice of the hyperparameters, training was performed by selecting the DNN parameters that minimize the RMSE metric (Eq. (A.3)) using the Adam optimizer (Kingma and Ba, 2014) with the observed streamflow as reference. The Nash Sutcliffe coefficient NS (Eq. (1)) was then computed on each one of the $k = 10$ groups selected as the test set. Considering that the NS coefficients depend on the hyperparameters, i.e. the number of hidden layers and neurons and the activation function, the above procedure was repeated with several combinations of hyperparameters selecting those that provided the highest NS values.

The resulting DNN model (i.e. the best combination of hyperparameters and the parameters learned with the training step) was then verified against the test set not used in the training and validation procedures (i..e, the 20% of the data not used in the k-fold procedure). The NS coefficient obtained in this step can be considered representative of the quality of the model.

The NS values of the training and test sets were 0.73 and 0.65 respectively, while in the cross-validation (k-fold) procedure an average NS of 0.73 was obtained with a standard deviation of 0.012 obtained across the $k = 10$ folds. With these performances, in particular the small reduction of NS between the training and test set, the model can be considered satisfactory and able to generalize without overfitting.

The final structure of the network was composed of four hidden layers each one with 14 neurons, in addition to the input and output layers. As activation function, we used the Exponential Linear Unit function (ELU) (Clevert et al., 2016):

$$g(z) = \begin{cases} \alpha(\exp(z) - 1), & \text{if } z > 0 \\ z, & \text{if } z \geq 0 \end{cases} \tag{B.1}$$

where α was set equal to one.

The DNN model was implemented by using the *Keras* deep-learning library (Chollet, 2018) developed in Python.

Appendix C. Variation in time of the glacier surface

The surface area of the glacier was obtained for the years 1980 (4.80 km^2), 1987 (4.57 km^2), 1990 (3.88 km^2), 2000 (3.02 km^2), 2003 (2.82 km^2), 2006 (2.35 km^2) and 2015 (1.39 km^2) by delimiting the glacier contour in the orthophoto maps provided by the Comitato Glaciologico Italiano and Meteotrentino (Carturan et al., 2013a). The value the glacier surface area assumed in 1958 was extracted from the paper by Carturan et al. (2013a). In the remaining years, the area was reconstructed as follows. First, the maximum thickness of the glacier at the above years was obtained by entering the surface area in the Area-Thickness relationship shown in Fig. C.1. The resulting values were used as a reference for computing the evolution of the maximum thickness s_i at the year i between two successive times at which the surface area was known (extracted from the orthophotos), as follows:

$$s_i = B_{n,i} \frac{(s_{i_1} - s_{i_2})}{\sum_{j=i_1+1}^{i_2} B_{n,j}}, \quad i = i_1 + 1, \ldots, i_2 \tag{C.1}$$

where $B_{n,i}$ is the glacier net balance at the year i (see Fig. 5) and i_1 and i_2 are the two successive years at which the area was determined from the orthophotos. The Expression (C.1) was used to compute the evolution of the maximum glacier thickness in the intervals 1980–1990, 1990–2000, and 2000–2006. Before 1980 and after 2006 the maximum thickness was obtained from the following expression:

$$s_i = s_{i-1} + \frac{B_{n,i}}{r_\rho} \tag{C.2}$$

where r_ρ is the ratio between the density of the ice and that of water, assumed here equal to 0.9 (Carturan et al., 2013a). We assumed the density of the ice as a reference because the glacier showed a negative net balance since the beginning of the time series, except in a few years between 1967 and 1980. In the period 1967–1980 the Eq. (C.2) was applied backward starting from $i = 1980$ and inverting it: $s_{i-1} = s_i - \frac{B_{n,i}}{r_\rho}$. On the other hand from 2006 to 2020 the Eq. (C.2) was used. The maximum glacier thickness was then used in the Area-Thickness graph of Fig. C.1 (solid line) to obtain the area of the glacier at all the years, except for those already computed from the orthophotos. The evolution in time of the glacier surface area is shown in Fig. C.1 with black bullets.

The relationship between the glacier area and the maximum glacier thickness was obtained by Martinelli et al. (2010) from the DTM of the glacier bedrock and the estimate of the 2008 glacier surface. The DTM was obtained by means of two GPR surveys conducted in 2007 and 2008 (Carturan et al., 2013a) and the glacier surface from the differential GPS survey conducted in the autumn of 2006 by the "Ufficio Previsione ed Organizzazione" of the Autonomous Province of Trento, Italy, taking into account the net glacier budget in the hydrological years 2006/2007 and 2007/2008 (Martinelli et al., 2010). The 2008 glacier surface was then moved up and down at steps of 0.1 m, and at each position the surface area was obtained by counting the number of cells of the DTM inside the contour of the glacier, determined by intersecting the translated surface with the bedrock.

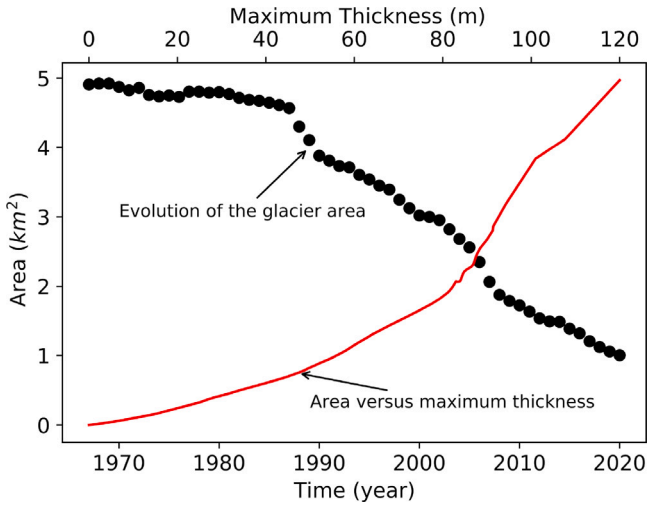

Fig. C.1. Surface area of the glacier versus its maximum thickness (red solid line) and time evolution of the glacier surface area (black bullets). (For interpretation of the references to color in this figure legend, the reader is referred to the web version of this article.)

Table D.7
Coupled measurements of flow rate and water stage at the Careser Baia gauging station used to obtain the rating curve.
Source: Data were provided by Meteotrentino.

ID	Date	h [m]	Q [m^3/s]
Baia 1	22-Jul-2009	0.15	1.135
Baia 3	22-Jul-2009	0.14	1.124
Baia 5	23-Jul-2009	0.19	1.705
Baia 6	23-Jul-2009	0.255	2.292
Baia 7	23-Jul-2009	0.295	2.733
Baia 8	23-Jul-2009	0.345	3.152
Baia 9	23-Jul-2009	0.4	3.942
Baia 10	13-Aug-2009	0.165	1.495
Baia 11	13-Aug-2009	0.28	2.476
Baia 12	13-Aug-2009	0.34	3.014
C2 Baia	21-Oct-2014	0.04	0.122
C1 Baia	21-Oct-2014	0.04	0.198
Baia 1–2019	25-Jul-2019	0.16	1.218
Baia 2–2019	25-Jul-2019	0.17	1.291
Baia Dilution 1	4-Jul-2018	0.12	1.043
Baia Dilution 2	4-Jul-2018	0.12	1.054
D1 Baia	18-Jul-2003	0.095	0.640
D2 Baia	18-Jul-2003	0.35	3.143
D3 Baia	18-Jul-2003	0.5	4.131
D4 Baia	18-Jul-2003	0.7	7.385

Appendix D. Rating curve of the Careser Baia gauging station

The rating curve was constructed by fitting the following power law expression: $Q = a\,h^b$ to the pairs of measured flow rate Q [m^3/s] and water stage h [m] provided by Meteotrentino (www.meteotrentino.it) and reported in Table D.7. The flow rate (water discharge) was measured by using the standard velocity-area method. In the years 2009 and 2019, the flow rate was evaluated by using the velocity-area method with the velocity measurements performed with an acoustic velocimeter (Sontek Flow Tracker). The same method was used in 2003, but no information is available on the type of instrument used to measure the stream velocity. In 2018 both measurements were conducted with the dilution method.

The solid red line of Fig. D.1 shows the rating curve obtained by using the entire set of data, while that represented by the solid blue line was obtained by repeating the fitting experiment after removing the last two measurements of Table D.7, indicated with a red bullet in the Figure.

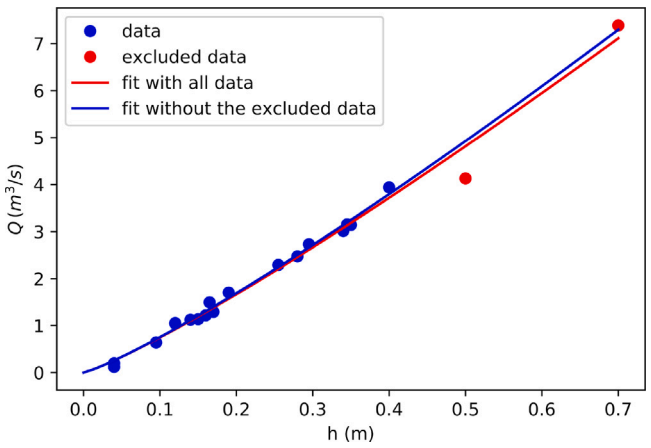

Fig. D.1. Rating curve at the Careser Baia gauging station (red solid line) obtained by fitting the power law expression $Q = a\,h^b$ to the experimental data shown in Table D.7. The solid blue line shows the fitting curve obtained after removing the last two measurements of the Table (identified by the red bullet). (For interpretation of the references to color in this figure legend, the reader is referred to the web version of this article.)

This was done to verify the consistency of these last two measurements performed at a high water stage with the other pairs. The two curves almost overlap, confirming that these two measurements are consistent with the others. In the present work, we used the rating curve obtained by using all the measurements and depicted with a red solid line in Fig. D.1 with the two parameters assuming the following values: $a = 10.7473\,[9.9632, 11.5314]$ and $b = 1.15787\,[1.08226, 1.233484]$. The values within the brackets indicate the 95% interval of confidence.

Appendix E. Supplementary data

Supplementary material related to this article can be found online at https://doi.org/10.1016/j.jhydrol.2023.130316.

References

Baraer, M., Mark, B.G., McKenzie, J.M., Condom, T., Bury, J., Huh, K.I., Portocarrero, C., Gómez, J., Rathay, S., 2012. Glacier recession and water resources in Peru's Cordillera Blanca. J. Glaciol. 58 (207), 134–150. http://dx.doi.org/10.3189/2012JoG11J186.

Barnett, T.P., Adam, J.C., Lettenmaier, D.P., 2005. Potential impacts of a warming climate on water availability in snow-dominated regions. Nature 438 (7066), 303. http://dx.doi.org/10.1038/nature04141.

Baroni, C., Bondesan, A., Chiarle, M., 2017. Report of the glaciological survey 2016. Geogr. Fisica Dinamica Quat. 40, 233–320. http://dx.doi.org/10.4461/GFDQ.2017.40.14.

Bavay, M., Grünewald, T., Lehning, M., 2013. Response of snow cover and runoff to climate change in high Alpine catchments of Eastern Switzerland. Adv. Water Resour. 55, 4–16. http://dx.doi.org/10.1016/j.advwatres.2012.12.009.

Beniston, M., 2003. Climatic change in mountain regions: a review of possible impacts. In: Climate Variability and Change in High Elevation Regions: Past, Present & Future. Springer, pp. 5–31.

Birsan, M.V., Molnar, P., Burlando, P., Pfaundler, M., 2005. Streamflow trends in Switzerland. J. Hydrol. 314 (1–4), 312–329. http://dx.doi.org/10.1016/j.jhydrol.2005.06.008.

Bliss, A., Hock, R., Radić, V., 2014. Global response of glacier runoff to twenty-first century climate change. J. Geophys. Res. Earth Surf. 119 (4), 717–730. http://dx.doi.org/10.1002/2013JF002931.

Bolibar, J., Rabatel, A., Gouttevin, I., Zekollari, H., Galiez, C., 2022. Nonlinear sensitivity of glacier mass balance to future climate change unveiled by deep learning. Nature Commun. 13 (1), 409. http://dx.doi.org/10.1038/s41467-022-28033-0.

Brown, L.E., Dickson, N.E., Carrivick, J.L., Füreder, L., 2015. Alpine river ecosystem response to glacial and anthropogenic flow pulses. Freshw. Sci. 34 (4), 1201–1215. http://dx.doi.org/10.1086/683062.

Brown, L.E., Hannah, D.M., Milner, A.M., 2007. Vulnerability of alpine stream biodiversity to shrinking glaciers and snowpacks. Global Change Biol. 13 (5), 958–966. http://dx.doi.org/10.1111/j.1365-2486.2007.01341.x.

Bunn, S.E., Arthington, A.H., 2002. Basic principles and ecological consequences of altered flow regimes for aquatic biodiversity. Environ. Manag. 30 (4), 492–507. http://dx.doi.org/10.1007/s00267-002-2737-0.

Carturan, L., Baroni, C., Becker, M., Bellin, A., Cainelli, O., Carton, A., Casarotto, C., Dalla Fontana, G., Godio, A., Martinelli, T., et al., 2013a. Decay of a long-term monitored glacier: Careser glacier (Ortles-Cevedale, European Alps). Cryosphere 7 (6), 1819–1838. http://dx.doi.org/10.5194/tc-7-1819-2013.

Carturan, L., Baroni, C., Brunetti, M., Carton, A., Dalla Fontana, G., Salvatore, M.C., Zanoner, T., Zuecco, G., 2016. Analysis of the mass balance time series of glaciers in the Italian Alps. Cryosphere 10 (2), 695–712. http://dx.doi.org/10.5194/tc-10-695-2016.

Carturan, L., De Blasi, F., Cazorzi, F., Zoccatelli, D., Bonato, P., Borga, M., Dalla Fontana, G., 2019. Relevance and scale dependence of hydrological changes in glacierized catchments: Insights from historical data series in the Eastern Italian Alps. Water 11 (1), http://dx.doi.org/10.3390/w11010089.

Carturan, L., Filippi, R., Seppi, R., Gabrielli, P., Notarnicola, C., Bertoldi, L., Paul, F., Rastner, P., Cazorzi, F., Dinale, R., et al., 2013b. Area and volume loss of the glaciers in the Ortles-Cevedale group (Eastern Italian Alps): controls and imbalance of the remaining glaciers. Cryosphere 7 (5), 1339–1359. http://dx.doi.org/10.5194/tc-7-1339-2013.

Carturan, L., Seppi, R., 2007. Recent mass balance results and morphological evolution of Careser Glacier (Central Alps). Geogr. Fisica Dinamica Quat. 30 (1), 33–42, URL: http://www.glaciologia.it/wp-content/uploads/FullText/full_text_30_1/04_Carturan_33_42.pdf.

Castagna, M., Bellin, A., 2009. A Bayesian approach for inversion of hydraulic tomographic data. Water Resour. Res. 45 (4), http://dx.doi.org/10.1029/2008WR007078.

Chollet, F., 2018. Deep Learning with Python. Manning Shelter Island, http://dx.doi.org/10.1007/978-1-4842-2766-4.

Clevert, D.A., Unterthiner, T., Hochreiter, S., 2016. Fast and accurate deep network learning by exponential linear units (ELUs). In: 4th International Conference on Learning Representations, ICLR 2016 - Conference Track Proceedings. pp. 1–14.

Collins, D.N., 2006. Climatic variation and runoff in mountain basins with differing proportions of glacier cover. Hydrol. Res. 37 (4–5), 315–326. http://dx.doi.org/10.2166/nh.2006.017.

Collins, D.N., 2008. Climatic warming, glacier recession and runoff from Alpine basins after the Little Ice Age maximum. Ann. Glaciol. 48 (1), 119–124. http://dx.doi.org/10.3189/172756408784700761.

Compagno, L., Eggs, S., Huss, M., Zekollari, H., Farinotti, D., 2021. Brief communication: Do 1.0, 1.5, or 2.0 ^{o}C matter for the future evolution of Alpine glaciers? Cryosphere 15 (6), 2593–2599. http://dx.doi.org/10.5194/tc-15-2593-2021, URL: https://tc.copernicus.org/articles/15/2593/2021/.

Conover, W.J., 1999. Practical Nonparametric Statistics. John Wiley & Sons, Wiley Series in Probability and Statistics: Applied Probability and Statistics Section.

Diks, C.G.H., Vrugt, J.A., 2010. Comparison of point forecast accuracy of model averaging methods in hydrologic applications. Stoch. Environ. Res. Risk Assess. 24, 809–820. http://dx.doi.org/10.1007/s00477-010-0378-z.

Dobler, A., Ahrens, B., 2008. Precipitation by a regional climate model and bias correction in Europe and South Asia. Meteorol. Z. 17 (4), 499–509. http://dx.doi.org/10.1127/0941-2948/2008/0306.

Eberhart, R., Kennedy, J., 1995. A new optimizer using particle swarmtheory. In: MHS'95. Proceedings of the Sixth International Symposium on Micro Machine and Human Science. pp. 39–43. http://dx.doi.org/10.1109/MHS.1995.494215.

Farinotti, D., Usselmann, S., Huss, M., Bauder, A., Funk, M., 2012. Runoff evolution in the Swiss Alps: projections for selected high-alpine catchments based on ENSEMBLES scenarios. Hydrol. Process. 26 (13), 1909–1924. http://dx.doi.org/10.1002/hyp.8276.

Galos, S.P., Klug, C., Prinz, R., Rieg, L., Sailer, R., Dinale, R., Kaser, G., 2015. Recent glacier changes and related contribution potential to river discharge in the vinschgau/val venosta, Italian alps. Geogr. Fis. Din. Quat. 38, 143–154. http://dx.doi.org/10.4461/GFDQ.2015.38.13.

Gobiet, A., Kotlarski, S., Beniston, M., Heinrich, G., Rajczak, J., Stoffel, M., 2014. 21st century climate change in the European Alps: a review. Sci. Total Environ. 493, 1138–1151. http://dx.doi.org/10.1016/j.scitotenv.2013.07.050.

Goodfellow, I., Bengio, Y., Courville, A., 2016. Deep Learning. MIT Press, http://www.deeplearningbook.org.

Goovaerts, P., et al., 1997. Geostatistics for Natural Resources Evaluation. Oxford University Press on Demand.

Grossi, G., Caronna, P., Ranzi, R., 2013. Hydrologic vulnerability to climate change of the Mandrone glacier (Adamello-Presanella group, Italian Alps). Adv. Water Resour. 55, 190–203. http://dx.doi.org/10.1016/j.advwatres.2012.11.014.

Grossi, G., Lendvai, A., Peretti, G., Ranzi, R., 2017. Snow Precipitation Measured by Gauges: Systematic Error Estimation and Data Series Correction in the Central Italian Alps. Water 9 (7), http://dx.doi.org/10.3390/w9070461.

Gurnell, A., Clark, M., Hill, C., 1992. Analysis and interpretation of patterns within and between hydroclimatological time series in an alpine glacier basin. Earth Surf. Process. Landf. 17 (8), 821–839. http://dx.doi.org/10.1002/esp.3290170808.

Haeberli, W., Hoelzle, M., Paul, F., Zemp, M., 2007. Integrated monitoring of mountain glaciers as key indicators of global climate change: the European Alps. Ann. Glaciol. 46 (1), 150–160. http://dx.doi.org/10.3189/172756407782871512.

Höge, M., Guthke, A., Nowak, W., 2019. The hydrologist's guide to Bayesian model selection, averaging and combination. J. Hydrol. 572, 96–107. http://dx.doi.org/10.1016/j.jhydrol.2019.01.072.

Hugonnet, R., McNabb, R., Berthier, E., Menounos, B., Nuth, C., Girod, L., Farinotti, D., Huss, M., Dussaillant, I., Brun, F., Kääb, A., 2021. Accelerated global glacier mass loss in the early twenty-first century. Nature 592, 726–731. http://dx.doi.org/10.1038/s41586-021-03436-z.

Huss, M., 2011. Present and future contribution of glacier storage change to runoff from macroscale drainage basins in Europe. Water Resour. Res. 47 (7), http://dx.doi.org/10.1029/2010WR010299.

Huss, M., 2012. Extrapolating glacier mass balance to the mountain range scale: the European Alps 1900–2100. Cryosphere Discuss. 6, 1117–1156. http://dx.doi.org/10.5194/tc-6-713-2012.

Huss, M., Farinotti, D., Bauder, A., Funk, M., 2008. Modelling runoff from highly glacierized alpine drainage basins in a changing climate. Hydrol. Process. 22 (19), 3888–3902. http://dx.doi.org/10.1002/hyp.7055.

Huss, M., Hock, R., 2015. A new model for global glacier change and sea-level rise. Front. Earth Sci. 3, http://dx.doi.org/10.3389/feart.2015.00054, URL: https://www.frontiersin.org/articles/10.3389/feart.2015.00054.

Huss, M., Hock, R., 2018. Global-scale hydrological response to future glacier mass loss. Nature Clim. Change 8 (2), 135–140. http://dx.doi.org/10.1038/s41558-017-0049-x.

Hussain, M., 2020. pyHomogeneity. https://pypi.org/project/pyhomogeneity/1.1/.

Hussain, M., 2023. pymannkendall. https://pypi.org/project/pymannkendall/.

Hussain, M., Mahmud, I., 2019-07-25. pyMannKendall: a python package for non parametric Mann Kendall family of trend tests. J. Open Source Softw. 4 (39), 1556. http://dx.doi.org/10.21105/joss.01556.

Immerzeel, W.W., Lutz, A.F., Andrade, M., Bahl, A., Biemans, H., Bolch, T., Hyde, S., Brumby, S., Davies, B.J., Elmore, A.C., Emmer, A., Feng, M., Fernández, A., Haritashya, U., Kargel, J.S., Koppes, M., Kraaijenbrink, P.D.A., Kulkarni, A.V., Mayewski, P.A., Nepal, S., Pacheco, P., Painter, T.H., Pellicciotti, F., Rajaram, H., Rupper, S., Sinisalo, A., Shrestha, A.B., Viviroli, D., Wada, Y., Xiao, C., Yao, T., Baillie, J.E.M., 2020. Importance and vulnerability of the world's water towers. Nature 577 (7790), 364–369. http://dx.doi.org/10.1038/s41586-019-1822-y.

IPCC, 2023. AR6 Synthesis Report Climate Change 2023: Longer Report. The Intergovernmental Panel on Climate Change, URL: https://www.ipcc.ch/report/ar6/syr/.

Jacobsen, D., Milner, A.M., Brown, L.E., Dangles, O., 2012. Biodiversity under threat in glacier-fed river systems. Nature Clim. Change 2 (5), 361. http://dx.doi.org/10.1038/nclimate1435.

Jakob Themeßl, M., Gobiet, A., Leuprecht, A., 2011. Empirical-statistical downscaling and error correction of daily precipitation from regional climate models. Int. J. Climatol. 31 (10), 1530–1544. http://dx.doi.org/10.1002/joc.2168.

James D. Miller, G.R., 2012. Climate change impacts on glacier hydrology and river discharge in the Hindu Kush–Himalayas. Mt. Res. Dev. 32 (4), 461–467. http://dx.doi.org/10.1659/MRD-JOURNAL-D-12-00027.1.

Jansson, P., Hock, R., Schneider, T., 2003. The concept of glacier storage: a review. J. Hydrol. 282 (1), 116–129. http://dx.doi.org/10.1016/S0022-1694(03)00258-0.

Jiskoot, H., Mueller, M.S., 2012. Glacier fragmentation effects on surface energy balance and runoff: field measurements and distributed modelling. Hydrol. Process. 26 (12), 1861–1875. http://dx.doi.org/10.1002/hyp.9288.

Jost, G., Moore, R.D., Menounos, B., Wheate, R., 2012. Quantifying the contribution of glacier runoff to streamflow in the upper Columbia River Basin, Canada. Hydrol. Earth Syst. Sci. 16 (3), 849–860. http://dx.doi.org/10.5194/hess-16-849-2012.

Kingma, D.P., Ba, J., 2014. Adam: A method for stochastic optimization. In: Published as a Conference Paper at the 3rd International Conference for Learning Representations (ICLR). https://arxiv.org/abs/1412.6980v9.

Koboltschnig, G.R., Schöner, W., Zappa, M., Kroisleitner, C., Holzmann, H., 2008. Runoff modelling of the glacierized Alpine Upper Salzach basin (Austria): Multi-criteria result validation. Hydrol. Process. 22 (19), 3950–3964. http://dx.doi.org/10.1002/hyp.7112.

Kormann, C., Francke, T., Renner, M., Bronstert, A., 2015. Attribution of high resolution streamflow trends in Western Austria - an approach based on climate and discharge station data. Hydrol. Earth Syst. Sci. 19 (3), 1225–1245. http://dx.doi.org/10.5194/hess-19-1225-2015.

Krieger, S., Freij, N., Brazhe, A., Torrence, C., Compo, G.P., contributors, 2023. pyCWT. https://pycwt.readthedocs.io/en/latest/index.html.

Kuhn, M., Batlogg, N., 1998. Glacier runoff in Alpine headwaters in a changing climate. Int. Assoc. Hydrol. Sci. Publ. (248), 79–88.

Kumar, P., 2020. bias-correction. https://pypi.org/project/bias-correction/.

Kure, S., Jang, S., Ohara, N., Kavvas, M.L., Chen, Z.Q., 2013. Hydrologic impact of regional climate change for the snowfed and glacierfed river basins in the Republic of Tajikistan: hydrological response of flow to climate change. Hydrol. Process. 27 (26), 4057–4070. http://dx.doi.org/10.1002/hyp.9535.

Laurent, L., Buoncristiani, J.F., Pohl, B., Zekollari, H., Farinotti, D., Huss, M., Mugnier, J.L., Pergaud, J., 2020. A Bayesian approach for inversion of hydraulic tomographic data. In: The Impact of Climate Change and Glacier Mass Loss on the Hydrology in the Mont-Blanc Massif, Vol. 10, No. 1. http://dx.doi.org/10.1038/s41598-020-67379-7.

Lencioni, V., Stella, E., Zanoni, M.G., Bellin, A., 2022. On the delay between water temperature and invertebrate community response to warming climate. Sci. Total Environ. 837, 155759. http://dx.doi.org/10.1016/j.scitotenv.2022.155759.

Majone, B., Villa, F., Deidda, R., Bellin, A., 2016. Impact of climate change and water use policies on hydropower potential in the south-eastern Alpine region. Sci. Total Environ. 543, 965–980. http://dx.doi.org/10.1016/j.scitotenv.2015.05.009.

Mallucci, S., Bruno, M., Alberto, B., 2019. Detection and attribution of hydrological changes in a large alpine river basin. J. Hydrol. 575, 1214–1229. http://dx.doi.org/10.1016/j.jhydrol.2019.06.020.

Martinelli, T., Cainelli, O., Bellin, A., Becker, M.W., Bal, G., Godio, A., 2010. Caratterizzazione del substrato roccioso del ghiacciaio del Careser. Report, Università degli studi di Trento – Dipartimento Ingegneria Civile e Ambientale, p. 32 (in Italian).

Marzeion, B., Hock, R., Anderson, B., Bliss, A., Champollion, N., Fujita, K., Huss, M., Immerzeel, W.W., Kraaijenbrink, P., Malles, J.H., Maussion, F., Radić, V., Rounce, D.R., Sakai, A., Shannon, S., van de Wal, R., Zekollari, H., 2020. Partitioning the uncertainty of ensemble projections of global glacier mass change. Earth's Future 8 (7), http://dx.doi.org/10.1029/2019EF001470, e2019EF001470.

MeteoTrentino, 2023. https://www.meteotrentino.it/index.html#!/home.

Michel, A., Brauchli, T., Lehning, M., Schaefli, B., Huwald, H., 2020. Stream temperature and discharge evolution in Switzerland<? xmltex\break? > over the last 50 years: annual and seasonal behaviour. Hydrol. Earth Syst. Sci. 24 (1), 115–142. http://dx.doi.org/10.5194/hess-24-115-2020.

Milner, A.M., Khamis, K., Battin, T.J., Brittain, J.E., Barrand, N.E., Füreder, L., Cauvy-Fraunié, S., Gíslason, G.M., Jacobsen, D., Hannah, D.M., Hodson, A.J., Hood, E., Lencioni, V., Ólafsson, J.S., Robinson, C.T., Tranter, M., Brown, L.E., 2017. Glacier shrinkage driving global changes in downstream systems. Proc. Natl. Acad. Sci. 114 (37), 9770–9778. http://dx.doi.org/10.1073/pnas.1619807114.

Nepal, S., 2016. Impacts of climate change on the hydrological regime of the Koshi river basin in the Himalayan region. J. Hydro-Environ. Res. 10, 76–89. http://dx.doi.org/10.1016/j.jher.2015.12.001.

O'Neel, S., Hood, E., Arendt, A., Sass, L., 2014. Assessing streamflow sensitivity to variations in glacier mass balance. Clim. Change 123 (2), 329–341. http://dx.doi.org/10.1007/s10584-013-1042-7.

Paul, F., Frey, H., Le Bris, R., 2011. A new glacier inventory for the European Alps from Landsat TM scenes of 2003: challenges and results. Ann. Glaciol. 52 (59), 144–152. http://dx.doi.org/10.3189/172756411799096295.

Paul, F., Haeberli, W., 2008. Spatial variability of glacier elevation changes in the Swiss Alps obtained from two digital elevation models. Geophys. Res. Lett. 35 (21), http://dx.doi.org/10.1029/2008GL034718.

Paul, F., Kääb, A., Maisch, M., Kellenberger, T., Haeberli, W., 2004. Rapid disintegration of Alpine glaciers observed with satellite data. Geophys. Res. Lett. 31 (21), L21402. http://dx.doi.org/10.1029/2004GL020816, L21402.

Pettitt, A., 1979. A non-parametric approach to the change-point problem. J. R. Stat. Soc. Ser. C. Appl. Stat. 28 (2), 126–135, URL: http://www.jstor.org/stable/2346729.

Piani, C., Haerter, J., Coppola, E., 2010. Statistical bias correction for daily precipitation in regional climate models over Europe. Theor. Appl. Climatol. 99, 187–192. http://dx.doi.org/10.1007/s00704-009-0134-9.

Poff, N.L., Zimmerman, J.K.H., 2010. Ecological responses to altered flow regimes: a literature review to inform the science and management of environmental flows. Freshw. Biol. 55 (1), 194–205. http://dx.doi.org/10.1111/j.1365-2427.2009.02272.x.

Rahman, K.U., Pham, Q.B., Jadoon, K.Z., Shahid, M., Kushwaha, D.P., Duan, Z., Mohammadi, B., Khedher, K.M., Anh, D.T., 2022. Comparison of machine learning and process-based SWAT model in simulating streamflow in the Upper Indus Basin. Appl. Water Sci. 12 (8), 178. http://dx.doi.org/10.1007/s13201-022-01692-6.

Raschka, S., 2015. Python Machine Learning. Packt publishing ltd.

RGI Consortium, 2017. Randolph Glacier Inventory - A Dataset of Global Glacier Outlines, Version 6. National Snow and Ice Data Center, http://dx.doi.org/10.7265/4m1f-gd79, URL: https://nsidc.org/data/NSIDC-0770/versions/6.

Schädler, B., Weingartner, R., 2010. Impact of climate change on water resources in the alpine regions of Switzerland. In: Alpine Waters. Springer, pp. 59–69. http://dx.doi.org/10.1007/978-3-540-88275-6_3.

Sen, P.K., 1968. Estimates of the regression coefficient based on Kendall's tau. J. Amer. Statist. Assoc. 63 (324), 1379–1389. http://dx.doi.org/10.2307/2285891.

Shen, C., 2018. A transdisciplinary review of deep learning research and its relevance for water resources scientists. Water Resour. Res. 54 (11), 8558–8593. http://dx.doi.org/10.1029/2018WR022643.

Torrence, C., Compo, G.P., 1998. A practical guide to wavelet analysis. Bull. Am. Meteorol. Soc. 79 (1), 61–78. http://dx.doi.org/10.1175/1520-0477(1998)079<0061:APGTWA>2.0.CO;2.

Torrence, C., Webster, P.J., 1998. The annual cycle of persistence in the El Niño/Southern Oscillation. Q. J. R. Meteorol. Soc. 124 (550), 1985–2004. http://dx.doi.org/10.1002/qj.49712455010.

Weather South Tyrol, 2023. https://weather.provinz.bz.it/default.asp.

Weber, M., Braun, L., Mauser, W., Prasch, M., 2010. Contribution of rain, snow-and icemelt in the Upper Danube discharge today and in the future. Geogr. Fisica Dinamica Quat. 33 (2), 221–230, URL: http://www.glaciologia.it/wp-content/uploads/FullText/full_text_33_2/12_GFDQ_33_2_Weber_221_230.pdf.

WGMS, 2017. Fluctuations of Glaciers Database. Technical Report ICSU(WDS) / IUGG(IACS)/ UNEP / UNESCO / WMO, World Glacier Monitoring Service, Zurich, Switzerland, http://dx.doi.org/10.5904/wgms-fog-2017-06.

Zanon, G., 1992. Venticinque anni di bilancio di massa del ghiacciaio del Careser (Alpi centrali), 1966-67/1990-91. Geogr. Fisica Dinamica Quat. 15, 215–219, URL: http://www.glaciologia.it/wp-content/uploads/FullText/full_text_15_1_2/30_GFDQ_15_1_2_Zanon_215_220.pdf.

Zekollari, H., Huss, M., Farinotti, D., 2019. Modelling the future evolution of glaciers in the European Alps under the EURO-CORDEX RCM ensemble. Cryosphere 13 (4), 1125–1146. http://dx.doi.org/10.5194/tc-13-1125-2019.

Zemp, M., Gärtner-Roer, I., Nussbaumer, S., Hüsler, F., Machguth, H., Mölg, N., Paul, F., Hoelzle, M., 2015. Global Glacier Change Bulletin No. 1 (2012–2013). Technical Report ICSU(WDS) / IUGG(IACS)/ UNEP / UNESCO / WMO, World Glacier Monitoring Service, Zurich, Switzerland.